

**Joint workshop meeting
ACTIVE AND PASSIVE SEISMICS
IN LATERALLY INHOMOGENEOUS MEDIA II
and
19th INTERNATIONAL WORKSHOP ON SEISMIC
ANISOTROPY**

ABSTRACT BOOK

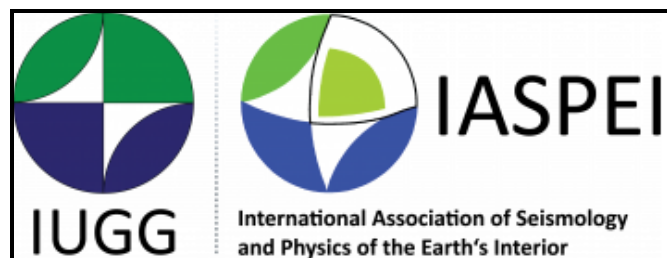


**Želiv Premonstratensian Monastery
Czech Republic
May 30 - June 3, 2022**

We are grateful to Seismik s.r.o. for their financial support of the event.



We are grateful to the European Association of Geoscientists & Engineers and the International Association of Seismology and Physics of the Earth's Interior for their help in advertizing the event.



Joint workshop meeting Active and passive seismics in laterally inhomogeneous media II and 19th International workshop on seismic anisotropy:

ABSTRACT BOOK

1st edition

Consortium "Seismic Waves in Complex 3-D Structures", Department of Geophysics, Faculty of Mathematics and Physics, Charles University, Ke Karlovu 3, Praha 2, Czech Republic
Prague, May 2022

ISBN 978-80-11-01592-3 (paperback)

ISBN 978-80-11-01593-0 (pdf)

**APSLIM/IWSA 2022
Programme of the Workshop**

Monday, May 30		
17:00	Departure of the bus from the Airport, Terminal 2	
17:15	Departure of the bus from Zličín, station M	
19:00	Estimated arrival to Želiv	
20:00	Icebreaker reception	
Tuesday, May 31		
8:00-9:00	Breakfast	Page
Morning session, chairman Leo Eisner		
9:00-9:35	Roger D. Borchardt: Implications of General Viscoelastic Ray Theory for Anelastic Geophysical Models	1
9:35-10:10	Luděk Klimeš: Extension of ray theory to anisotropic viscoelastic media	3
10:10-10:45	Ivan Pšenčík*, Veronique Farra: P-wave reflection moveout, spreading and reflection coefficient in a horizontally layered medium of arbitrary anisotropy	5
10:45-11:20	Coffee break	
11:20-11:55	James Ludlam*, Katy Tant, Victoria Dolean and Andrew Curtis: Fast 2D travel time fields and ray tracing calculations in strongly anisotropic media	7
11:55-12:30	Mengqi Li and Alexey Stovas*: On perturbation of eikonal equation in HTI models	9
12:40-14:00	Lunch	
Afternoon session, chairman Bjorn Ursin		
14:00-14:35	Václav Bucha: Kirchhoff pre-stack depth scalar migration using the prevailing-frequency approximation of the coupling ray theory	11
14:35-15:10	Maarten V. de Hoop: Advances in inverse problems in anisotropic elasticity for high-frequency waves	13
15:10-15:45	Lou Parkes: Seismic array analysis for the robust observation of anisotropy	15
15:45-16:20	Coffee break	
16:20-16:55	Ed Wright*, Chris Hanevel, René-Édouard Plessix: An example of multi parameter finite frequency tomography	17
16:55-17:30	T.J. Moser: Huygens' principle and diffraction - a complex history	20
18:00	Monastery excursion	
19:00	Dinner	
Wednesday, June 1		
8:00-9:00	Breakfast	
Morning session, chairman Alexey Stovas		
9:00-9:35	Petr Bulant* & Luděk Klimeš: Prevailing-frequency approximation of the coupling ray theory for S waves along the SH and SV reference rays	21
9:35-10:10	Kristoffer Tesdal Galtung* and Alexey Stovas: Diving waves in factorised orthorhombic media	23
10:10-10:45	Igor Ravve* and Zvi Koren: Slowness vector and ray velocity magnitude from ray direction in TTI media	25
10:45-11:20	Coffee break	
11:20-11:55	Björn Ursin* and Lasse Amundsen: On Richards' paradox	27
11:55-12:30	T.J. Moser: Update of diffraction imaging and modeling - methods and applications	29
12:40-14:00	Lunch	
14:00 - 19:00	Tour to UNESCO town Telč	
19:00	Barbecue	
Thursday, June 2		
8:00-9:00	Breakfast	
Morning session, chairman Igor Ravve		
9:00-9:35	Morten Jakobsen*, Ujjwal Shekar, Kui Xiang and Jakub W. Both: Simultaneous estimation of microseismic source parameters and velocity model using a Gauss-Newton consistent scattering approach	31
9:35-10:10	Maarten V. de Hoop: Anatomy of Mars SEIS data from deep learning	33
10:10-10:45	Ujjwal Shekhar*, Morten Jakobsen, Einar Iversen, Inga Berre: Fast integral equation method for micro-seismic waveform modeling	35
10:45-11:20	Coffee break	
11:20-11:55	Miłosz Wcisło*, František Staněk, František Gallovič, Shaojiang Wu and Ivan Pšenčík: Induced supershear microseismic event with rupture directivity and superimposed attenuation effects	37
11:55-12:30	Leo Eisner: Pore Pressure Mapping Using Microseismicity and Borehole Data	39
12:40-14:00	Lunch	
Afternoon session, chairman Tijmen Jan Moser		
14:00-14:35	Miłosz Wcisło*, Ivan Pšenčík and José Carcione: Comparison of ray and full-wave synthetic seismograms of reflected SH waves in attenuating media	41
14:35-15:10	Alexey Stovas*, Yuriy Roganov and Vyacheslav Roganov: The degenerate elastic orthorhombic models	43
15:10-15:45	Leon Thomsen* and Colin Sayers: Seismic anisotropy of fractured shales	45
15:45-16:20	Coffee break	
16:20-16:55	Leon Thomsen: The Logical Error in Gassmann Poroelectricity: Experimental Data	47
16:55-17:30	General discussion, votes for publication of Proceedings, votes for the next APSLIM/IWSA	
18:00	Monastery Brewery excursion	
19:00	Farewell party	
Friday, June 3		
8:00-9:00	Breakfast	
10:00	Bus departure from Želiv	
11:45	Estimated stop at Zličín	
12:00	Estimated arrival to the Prague Airport	

Implications of General Viscoelastic Ray Theory for Anelastic Geophysical Models

Roger D. Borchardt

U.S. Geological Survey

Recent advances in general viscoelastic ray theory provide a rigorous mathematical framework for purposes of inferring anelastic geophysical models. They provide closed-form solutions of forward ray-tracing and simple inverse problems for horizontal and spherical anelastic media. These solutions provide a number of insights regarding the characteristics of anelastic seismic waves and their ray paths not provided by conventional Q models. They account for changes in velocity and attenuation of anelastic P and S body waves associated with changes in inhomogeneity of the waves induced by anelastic material boundaries and gradients along the ray path. These changes, which are not induced at elastic boundaries, manifest themselves as variations in ray-path location, travel time, and amplitude attenuation as inferred at the surface of an anelastic Earth.

The forward ray-tracing solutions provide computation algorithms for general viscoelastic ray-tracing computer codes that can be used to exactly account for these variations in a variety of tomography-inferred anelastic geophysical models, such as those used to delineate the anelastic properties of the mantle and near-surface petroleum reserves. Numerical models indicate these distinctions increase with inhomogeneity of the waves and are more significant for some ray tracing problems than others. The solutions of inverse problems including that involving the viscoelastic solution of the Herglotz-Wiechert integral permit simultaneous inference of intrinsic-material seismic absorption and material wave speed from empirical travel-time and amplitude-attenuation curves. Application of these recent advances in general viscoelastic ray theory to large empirical teleseismic and exploration data sets will provide a host of research opportunities for the younger generation to advance our understanding of the anelastic properties of the Earth's interior and their interpretations. ([Borchardt, 2020, pp. 430-32, isbn=9781108495691](#)).

EXTENSION OF RAY THEORY TO ANISOTROPIC VISCOELASTIC MEDIA

Luděk Klimeš

*Department of Geophysics, Faculty of Mathematics and Physics, Charles University
Ke Karlovu 3, 121 16 Praha 2, Czech Republic, <http://sw3d.cz/staff/klimes.htm>*

Attenuation is a very important phenomenon in wave propagation, and is essential whenever the intensity of waves matters. It is thus fundamental to extend the ray theory from anisotropic elastic media to anisotropic viscoelastic media.

The idea of the extension looks simple: The eikonal equation in an attenuating medium has the form of a complex-valued Hamilton–Jacobi equation, which would generate complex-valued rays. Since we know the velocity model in real space rather than in complex space, we have to trace the real-valued reference rays using the reference Hamiltonian function, and calculate the complex-valued travel time right in real space by the perturbation from the reference travel time calculated along real-valued reference rays to the complex-valued travel time defined by the complex-valued Hamilton–Jacobi equation (Klimeš, 2002; 2016). Analogously for the corresponding amplitudes (Klimeš, 2006a). For this purpose, Klimeš & Klimeš (2011) designed the construction of the optimum real-valued reference Hamiltonian function corresponding to a given complex-valued Hamiltonian function.

However, we have encountered various more or less expected problems. The ray tracing equations and the corresponding equations of geodesic deviation (Červený, 1972) are often formulated in terms of the eigenvectors of the Christoffel matrix (Klimeš, 2006b). Unfortunately, a complex-valued Christoffel matrix need not have all three eigenvectors at an S-wave singularity (Klimeš, 2021). We thus have to formulate the ray tracing equations and the corresponding equations of geodesic deviation using the characteristic values of the complex-valued Christoffel matrix, without the eigenvectors of the Christoffel matrix (Klimeš, 2020). The resulting equations for the real-valued reference P-wave rays and real-valued reference common S-wave rays are applicable everywhere, including S-wave singularities.

The eigenvectors of the complex-valued Christoffel matrix are normalized to unit complex-valued pseudonorm with respect to pseudoscalar product $a_i b_i$ of vectors a_i and b_i rather than to unit real-valued norm with respect to scalar product $a_i^* b_i$, because the eigenvectors are pseudoorthogonal with respect to the pseudoscalar product (Klimeš, 2018). Consequently, the pseudonormal S-wave eigenvectors frequently diverge when approaching an S-wave singularity (Klimeš, 2022). This divergence does not occur in elastic media. As a result, the phase-space derivatives of the anisotropic-ray-theory Hamiltonian function used to trace the anisotropic-ray-theory rays may also diverge when approaching an S-wave singularity. Fortunately, the phase-space derivatives of the reference Hamiltonian function used to trace the reference common S-wave rays are smooth at S-wave singularities (Klimeš, 2020).

If the S-wave eigenvectors of the complex-valued Christoffel matrix diverge at an S-wave singularity, the corresponding anisotropic-ray-theory vectorial amplitudes diverge at the S-wave singularity too. This divergence does not occur in elastic media where the anisotropic-ray-theory vectorial amplitudes diverge at caustics only.

Since the variation of the S-wave eigenvectors along the reference ray plays a decisive role in the coupling equations (Bulant & Klimeš, 2002; Klimeš, 2013), the divergence of S-wave eigenvectors in a vicinity of an S-wave singularity represents a considerably challenging problem. The coupling equations for viscoelastic media contain the complex-valued angle of rotation of the S-wave eigenvectors about the P-wave eigenvector instead of the real-valued angle of rotation used in elastic media. Fortunately, these coupling equations for viscoelastic media compensate the divergence of S-wave eigenvectors and yield vectorial amplitudes smoothly varying through S-wave singularities. Whereas the coupling ray theory corrects just the S-wave polarization in elastic media, it corrects also the S-wave amplitudes at S-wave singularities in viscoelastic media which may diverge in the anisotropic ray theory.

Acknowledgements

The research has been supported by the Czech science foundation under contract 20-06887S, and by the members of the consortium “Seismic Waves in Complex 3-D Structures” (see “<http://sw3d.cz>”).

References

- Bulant, P. & Klimeš, L. (2002): Numerical algorithm of the coupling ray theory in weakly anisotropic media. *Pure appl. Geophys.*, **159**, 1419–1435.
- Červený, V. (1972): Seismic rays and ray intensities in inhomogeneous anisotropic media. *Geophys. J. R. astr. Soc.*, **29**, 1–13.
- Klimeš, L. (2002): Second-order and higher-order perturbations of travel time in isotropic and anisotropic media. *Stud. geophys. geod.*, **46**, 213–248.
- Klimeš, L. (2006a): Spatial derivatives and perturbation derivatives of amplitude in isotropic and anisotropic media. *Stud. geophys. geod.*, **50**, 417–430.
- Klimeš, L. (2006b): Common-ray tracing and dynamic ray tracing for S waves in a smooth elastic anisotropic medium. *Stud. geophys. geod.*, **50**, 449–461.
- Klimeš, L. (2013): Coupling ray series. *Stud. geophys. geod.*, **57**, 253–266.
- Klimeš, L. (2016): Transformation of spatial and perturbation derivatives of travel time at a curved interface between two arbitrary media. *Stud. geophys. geod.*, **60**, 451–470.
- Klimeš, L. (2018): Frequency-domain ray series for viscoelastic waves with a non-symmetric stiffness matrix. *Stud. geophys. geod.*, **62**, 261–271.
- Klimeš, L. (2020): Tracing real-valued reference rays in anisotropic viscoelastic media. *Seismic Waves in Complex 3-D Structures*, **30**, 77–94.
- Klimeš, L. (2021): Two S-wave eigenvectors of the Christoffel matrix need not exist in anisotropic viscoelastic media. *Stud. geophys. geod.*, **65**, 291–295.
- Klimeš, L. (2022): S-wave polarization vectors in anisotropic viscoelastic media. *Seismic Waves in Complex 3-D Structures*, **31**, 69–87.
- Klimeš, M. & Klimeš, L. (2011): Perturbation expansions of complex-valued traveltimes along real-valued reference rays. *Geophys. J. int.*, **186**, 751–759.
- The references are available online at “<http://sw3d.cz>”.

**P-WAVE REFLECTION MOVEOUT, SPREADING
AND REFLECTION COEFFICIENT
IN A HORIZONTALLY LAYERED MEDIUM
OF ARBITRARY ANISOTROPY**

Ivan Pšenčík ^{1,2)}, Véronique Farra ³⁾

¹⁾Institute of Geophysics, Acad. Sci. of Czech Republic, Boční II, 141 31 Praha 4, Czech Republic, ip@ig.cas.cz

²⁾Charles University, Faculty of Mathematics and Physics, Department of Geophysics, Ke Karlovu 3, 121 16 Praha 2, Czech Republic

³⁾Université Paris Cité, Institut de Physique du Globe, Paris, France, farra@ipgp.fr

We present and test approximate formulae for P-wave reflection moveout, geometrical spreading and reflection coefficient in horizontally layered anisotropic media of arbitrary symmetry and orientation. The formulae are based on weak-anisotropy approximation and expressed in terms of A-parameters (Pšenčík et al., 2018). A-parameters form a set of 21 parameters, which represent an alternative to 21 independent elements of the stiffness tensor c_{ijkl} or elastic parameters $C_{\alpha\beta}$ in the Voigt notation. For the derivation of the approximate reflection coefficient of the unconverted P wave, weak-contrast approximation is also used.

The approximate moveout formula of the unconverted P wave reflected at the bottom of a stack of horizontal layers and recorded along an arbitrarily selected profile has the form (Farra and Pšenčík, 2020):

$$T^2(x) = \left[\sum_{i=1}^N T_i(x_i) \right]^2, \quad x = \sum_{i=1}^N x_i. \quad (1)$$

Here T is the travelttime of the reflected wave at the offset x . N is the number of layers. T_i and x_i are the travelttime and offset corresponding to the down- and up-going elements of the ray of the reflected wave in the i -th layer. With the use of two approximations: (1) the replacement of the actual ray by a ray in a reference isotropic medium and (2) the replacement of the exact ray velocity by its first-order weak-anisotropy approximation, the travelttime T_i reads:

$$T_i^2(\bar{x}_i) = T_{0i}^2(1 + \bar{x}_i^2)^3 / P(\bar{x}_i). \quad (2)$$

Here, $T_{0i} = 2h_i/\alpha_i$ and $\bar{x}_i = x_i/2h_i$ are two-way zero-offset travelttime and normalized offset in the i -th layer, h_i and α_i are the thickness and the P-wave reference velocity of the i -th layer. The symbol $P(\bar{x}_i)$ in equation (2) denotes the polynomial:

$$P(\bar{x}) = (1 + \bar{x}^2)^2 + 2\epsilon_x^P \bar{x}^4 + 2(\eta_y^P + \epsilon_x^P + \epsilon_z^P) \bar{x}^2 + 2\epsilon_z^P. \quad (3)$$

In equation (3), ϵ_x^P , ϵ_z^P and η_y^P are the profile A-parameters, which can be expressed as linear functions of 9 global A-parameters defined in the global coordinate system or functions of (number dependent on the symmetry of the considered anisotropy) crystal A-parameters defined in the coordinate system coinciding with the symmetry elements of the considered anisotropy.

As shown by Farra and Pšenčík (2021), the geometrical spreading of unconverted P wave reflected at the bottom of a stack of horizontal layers of varying arbitrary anisotropy

can be expressed in the first-order weak-anisotropy approximation in the factorized form:

$$L(x, \varphi) = L_{\parallel}(x, \varphi)L_{\perp}(x, \varphi) . \quad (4)$$

Here

$$L_{\parallel}(x, \varphi) = \cos \psi \left(\frac{\partial^2 T}{\partial x^2} \right)^{-1/2} , \quad L_{\perp}(x, \varphi) = x \left(\frac{\partial^2 T}{\partial \varphi^2} + x \frac{\partial T}{\partial x} \right)^{-1/2} . \quad (5)$$

Here φ is the azimuth of the source-receiver profile and ψ is the ray angle of the reference ray. $T = T(x, \varphi)$ is the travelttime given by equations (1)-(3).

Approximate reflection coefficient of unconverted P wave has the form (Pšenčík and Farra, 2022):

$$R_{PP}(\theta_i) = R_{PP}^{iso}(\theta_i) + \frac{1}{2} \Delta \epsilon_z^P + \frac{1}{2} (\Delta \delta_y^P - 8 \frac{\bar{\beta}^2}{\bar{\alpha}^2} \Delta \gamma_y^P - \Delta \epsilon_z^P) \sin^2 \theta_i + \frac{1}{2} \Delta \epsilon_x^P \sin^2 \theta_i \tan^2 \theta_i . \quad (6)$$

The symbol R_{PP}^{iso} denotes the P-wave reflection coefficient in the reference model, in which the two half-spaces are isotropic. It reads:

$$R_{PP}^{iso}(\theta_i) = \frac{1}{2} \frac{\Delta Z}{\bar{Z}} + \frac{1}{2} \left[\frac{\Delta \alpha}{\bar{\alpha}} - 4 \frac{\bar{\beta}^2}{\bar{\alpha}^2} \frac{\Delta G}{\bar{G}} \right] \sin^2 \theta_i + \frac{1}{2} \frac{\Delta \alpha}{\bar{\alpha}} \sin^2 \theta_i \tan^2 \theta_i . \quad (7)$$

The angle θ_i is the angle of incidence, symbols Z and G are $Z = \rho \alpha$ and $G = \rho \beta^2$, respectively. The symbol Δ denotes contrast across the reflector, bar symbol an average.

The moveout formula $T(x)$ and the in-line spreading $L_{\parallel}(x, \varphi)$ depend on 3, the out-of-plane spreading $L_{\perp}(x, \varphi)$ depends on 6 profile A-parameters in each layer. Through the Bond transformation, the moveout and spreading formulae depend on 9 global A-parameters in each layer. P-wave reflection coefficient depends on contrast of 4 profile A-parameters or, through the Bond transformation, on contrast of 12 global A-parameters. No non-physical approximation such as acoustic approximation is used. On numerical tests, we illustrate the accuracy of the given approximate formulae.

Acknowledgement

We are grateful to the project Seismic waves in complex 3-D structures (SW3D) and the Research Project 20-06887S of the Grant Agency of the Czech Republic for support.

References

Farra, V., and Pšenčík, I., 2020, P-wave reflection-moveout approximation for horizontally layered media of arbitrary moderate anisotropy. *Geophysics*, **85**, C61–C70.

Farra, V., and Pšenčík, I. 2021. Weak-anisotropy approximation of P-wave geometrical spreading in horizontally layered anisotropic media of arbitrary symmetry: Tilted transversely isotropic specification. *Geophysics*, **86**, C119–C132.

Pšenčík, I., Růžek, B., Lokajíček, T., and Svitek, T., 2018. Determination of rocksample anisotropy from P and Swave travelttime inversion. *Geophys. J. Int.*, **214**, 1088-1104.

Pšenčík, I., and Farra, V., 2022. Weak-anisotropy approximation of P-wave reflection coefficient in anisotropic media of arbitrary symmetry. *Geophysics*, **87**, C39–C48.

FAST 2D TRAVEL TIME FIELDS AND RAY TRACING CALCULATIONS IN STRONGLY ANISOTROPIC MEDIA

James Ludlam¹, Katy Tant¹, Victoria Dolean¹, and Andrew Curtis²

¹University of Strathclyde

²University of Edinburgh

Many inversion techniques used for travel time tomography require fast and accurate calculations of travel times as they must be run many times. Travel times in anisotropic elastic media are determined by solving the eikonal equation, often using a finite difference approach. Many such techniques work well in weakly anisotropic media, but perform poorly with strong anisotropy. For strongly anisotropic media the Anisotropic Multi-Stencil Fast Marching Method [1] (AMSFMM) has been used. This method is an extension of the fast marching method [2] which calculates travel time fields in isotropic media. Unfortunately results from this method can have a large bias in some directions (see Figure 1) making ray tracing through the travel time fields difficult.

We introduce a fast marching method, in which a finite-difference(FD) method approximates the wavefront as locally planar in each finite-difference stencil [3]. These wavefront estimates are used to calculate travel times at neighbouring points. As the FD grid becomes finer, this approximation of the wave front becomes more accurate, as do the travel times. Due to high wavefront curvatures around the source, we use a finer grid around the source to initiate wave propagation. This FD method is faster than that used in AMSFMM. We define materials at each grid point using phase velocity curves or alternatively with elastic stiffness tensors and density for any orthotropic material. The elastic stiffness tensors and density are used to solve the Christoffel equation at run time to obtain group and phase velocities for a small increase in computation in comparison to defining materials using velocity curves. This is useful in situations where there are many materials of interest, as we do not have to calculate the full velocity curve for all angles which we would otherwise do.

Using calculated travel time fields, we infer the fastest ray path from source to receiver using a new approach, which finds points where the ray path crosses a series of planes, iteratively progressing away from the source. The location and orientation of the planes is dependent upon the previous section of the ray which allows complex paths to be traced. Travel times can be obtained by integrating along the ray paths, and these are often more accurate than those obtained directly from the travel time fields. These ray paths can be used to obtain

derivatives of travel times with respect to local medium velocities, which enables the efficient use of gradient based inversion methods.

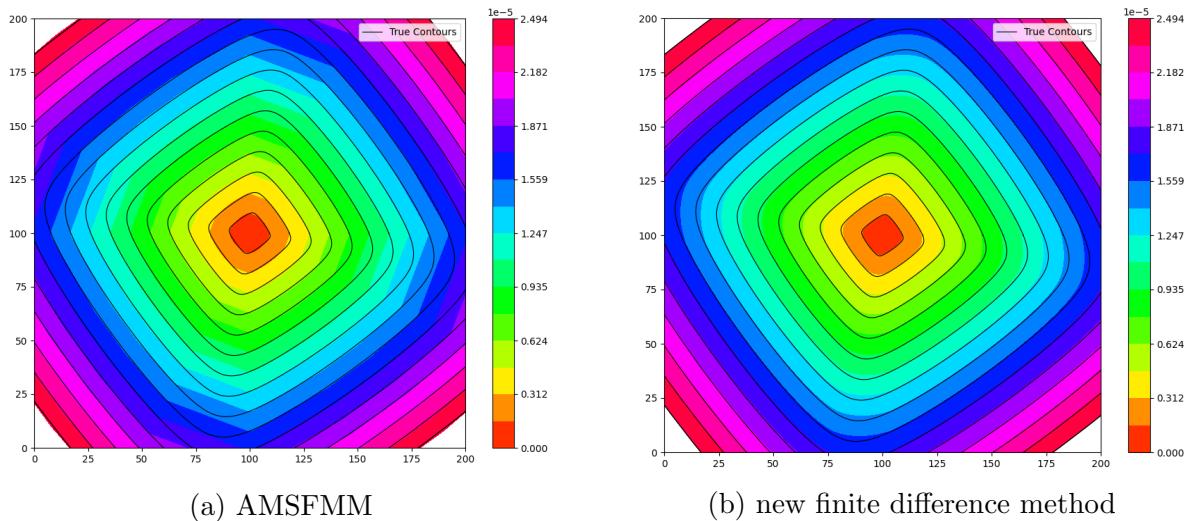


Figure 1: Contours of travel time field with true contours (black) for homogeneous media with an anisotropic orientations of 36° .

References

- [1] K. M. M. Tant, E. Galetti, A. J. Mulholland, A. Curtis, and A. Gachagan. Effective grain orientation mapping of complex and locally anisotropic media for improved imaging in ultrasonic non-destructive testing. *Inverse Problems in Science and Engineering*, 28(12):1694–1718, 2020.
- [2] J. A. Sethian. Fast Marching Methods. *SIAM Review*, 41(2):199–235, 1999.
- [3] David W. S. Eaton. Finite Difference Traveltime Calculation For Anisotropic Media. *Geophysical Journal International*, 114(2):273–280, August 1993.

ON PERTURBATION OF EIKONAL EQUATION IN HTI MODELS

Mengqi Li (NTNU, Norway) and Alexey Stovas (NTNU, Norway)

Introduction

The eikonal equations for transversely isotropic media are the complex quartic partial differential equation and cause instability for traveltimes inversion. The phenomenon of shear wave splitting in that medium with a horizontal symmetry axis (HTI) not only provides more information for inversion, but also enhances the computation consumption. Therefore, based on the perturbation theory, we approximate the P, SV, and SH wave traveltimes in terms of fracture weakness to apply for fracture parameters inversion. Similar approach was used by Alkhalifah (2002) who developed a linearized eikonal equation for perturbations in anelliptical parameter η to improve the traveltimes computation efficiency. Combining with the trial solutions of traveltimes by Taylor series in terms of η , Alkhalifah (2011) used the perturbation theory to expand the approximation of P-wave traveltimes under an elliptical background assumption for the transversely isotropic media with a vertical symmetry axis (VTI). Thus, the calculation of traveltimes is reduced from solving one fourth-order eikonal PDE to solving one second-order PDE for the elliptical background and three first-order PDEs for the coefficients of η , which accelerate the traveltimes computation. The similar method was also applied for a transversely isotropic medium with tilted (Stovas and Alkhalifah, 2012) and orthorhombic (Stovas, 2016) symmetry axes.

We derive the simple and accurate approximation under the homogeneous assumption and analyze the sensitivity of first- and second-order fracture weakness coefficients on traveltimes. To improve the accuracy of our approximation, we also expand the approximation of P-wave traveltimes with respect to anelliptical parameter η in the elliptical background, which was proved by the error test.

Theory

First, to the fractured medium, we have the stiffness coefficients in terms of weaknesses:

$$\begin{aligned} c_{11} &= c_{110}(1 - \Delta_N), \quad c_{13} = (c_{110} - 2c_{440})(1 - \Delta_N), \quad c_{33} = c_{110} \left[1 - \left((c_{110} - 2c_{440}) / c_{110} \right)^2 \Delta_N \right], \\ c_{55} &= c_{66} = c_{440}(1 - \Delta_T), \quad c_{23} = c_{33} - 2c_{44}, \quad c_{44} = c_{440}, \end{aligned} \quad (1)$$

where c_{110} and c_{440} are the stiffness coefficients for isotropic background and Δ_N and Δ_T are fracture normal and tangential weaknesses. The characteristic Christoffel equation in HTI medium is decoupled into SH and P-SV factors and given by

$$F(p_1, p_2, p_3; \Delta_N, \Delta_T) = F_{SH}(p_1, p_2, p_3; \Delta_N, \Delta_T) F_{PSV}(p_1, p_2, p_3; \Delta_N, \Delta_T) = 0, \quad (2)$$

where p_j , $j=1,2,3$ are projections of the slowness vector. By replacing the slowness projections with corresponding derivatives of eikonal, we define the second-order perturbation series in terms of fracture weaknesses,

$$\tau(x, y, z) = \tau_0 \left[1 + a_{10}\Delta_N + a_{01}\Delta_T + a_{20}\Delta_N^2 + 2a_{11}\Delta_N\Delta_T + a_{02}\Delta_T^2 \right], \quad (3)$$

where $\tau_0 = \tau_0(x, y, z)$ is the zero-order coefficient which is the traveltimes in a homogeneous medium, and $a_{ij} = a_{ij}(x, y, z)$ are corresponding perturbation coefficients. By equating the terms with the same order of fracture weaknesses, we obtain the equations for the first-order perturbation coefficients,

$$\frac{\partial a_{ij}}{\partial x} \frac{\partial \tau_0}{\partial x} + \frac{\partial a_{ij}}{\partial y} \frac{\partial \tau_0}{\partial y} + \frac{\partial a_{ij}}{\partial z} \frac{\partial \tau_0}{\partial z} = f_{ij} \left(\frac{\partial \tau_0}{\partial x}, \frac{\partial \tau_0}{\partial y}, \frac{\partial \tau_0}{\partial z} \right), \quad (4)$$

and the second-order perturbation coefficients,

$$\frac{\partial a_{kl}}{\partial x} \frac{\partial \tau_0}{\partial x} + \frac{\partial a_{kl}}{\partial y} \frac{\partial \tau_0}{\partial y} + \frac{\partial a_{kl}}{\partial z} \frac{\partial \tau_0}{\partial z} = g_{kl} \left(\frac{\partial \tau_0}{\partial x}, \frac{\partial \tau_0}{\partial y}, \frac{\partial \tau_0}{\partial z}, \frac{\partial a_{ij}}{\partial x}, \frac{\partial a_{ij}}{\partial y}, \frac{\partial a_{ij}}{\partial z} \right), \quad (5)$$

where f_{ij} and g_{kl} are functions of the first-order derivatives of $\tau_0(x, y, z)$.

We can also perform the perturbation of elliptical background,

$$\tau(x, y, z) = \tau_0 \left[1 + \sum_{j=1,2} m_j \eta^j \right]. \quad (6)$$

For a homogeneous HTI model, the perturbation coefficients are given by very simple expressions.

The accuracy of perturbation series can be improved by applying the Shanks transform.

In Figure 1 (top), we can see the relative error of linear and quadratic approximations and Shanks transform for P wave computed from perturbation series (3) for HTI model with $v_{p0} = 2 \text{ km/s}$, $\gamma = 0.5$ and

$$\Delta_N = \Delta_T = 0.2.$$

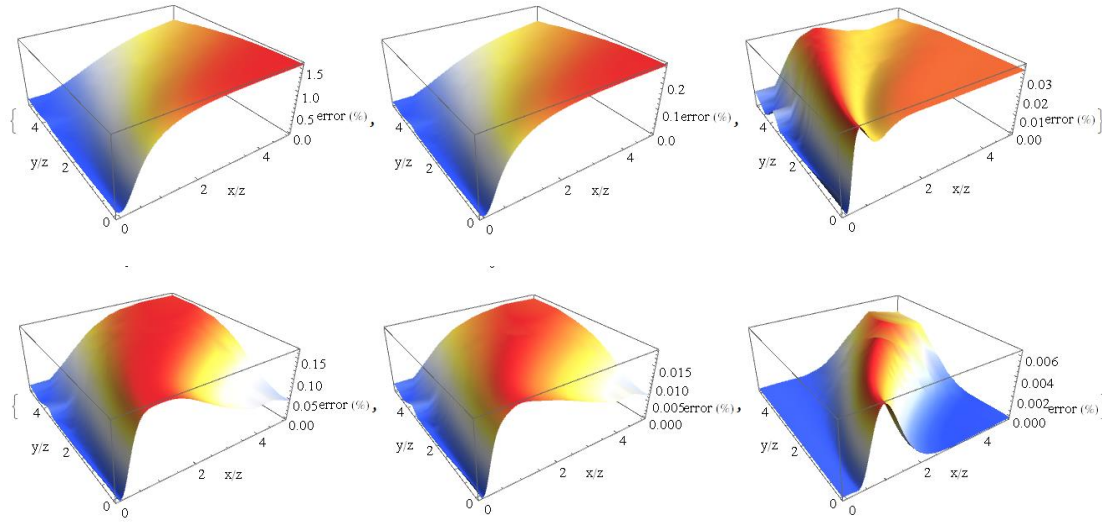


Figure 1. The relative error of linear and quadratic approximations and Shanks transform for P wave computed from perturbation series (3)(top) and (6) (bottom) for HTI model with $v_{p0} = 2 \text{ km/s}$, $\gamma = 0.5$ and

$$\Delta_N = \Delta_T = 0.2.$$

In Figure 1 (bottom), we can see the relative error of linear and quadratic approximations and Shanks transform for P wave computed from perturbation series (6) for HTI model mentioned above.

Conclusions

We define the perturbation series for eikonal equation in HTI model. The perturbation-based approximations for traveltimes in a homogeneous model are very accurate.

Acknowledgements

Alexey Stovas acknowledges the GAMES project for financial support.

References

- Alhalifah, T., 2002, Travelttime computation with the linearized eikonal equation for anisotropic media, *Geophysical Prospecting* **50**, 373-382.
- Alhalifah, T., 2011, Travelttime approximations for transversely isotropic media with an inhomogeneous background, *Geophysics* **76**, no.3, WA31-WA42.
- Stovas, A., and Alhalifah, T., 2012, A new travelttime approximation in TTI media, *Geophysics* **77**, no.4, C37-C42.
- Stovas, A., Masmoudi, N., and T.Alhalifah, 2016, Application of perturbation theory for P-wave eikonal equation in orthorhombic media, *Geophysics* **81**, no.6, C309-C317.

KIRCHHOFF PRE-STACK DEPTH SCALAR MIGRATION USING THE PREVAILING-FREQUENCY APPROXIMATION OF THE COUPLING RAY THEORY

Václav Bucha

Department of Geophysics, Faculty of Mathematics and Physics, Charles University,
Ke Karlovu 3, 121 16 Praha 2, Czech Republic

It is known that the isotropic ray theory assumes equal velocities of both S wave polarizations and the anisotropic ray theory assumes both S wave polarizations strictly decoupled (e.g. Bulant & Klimeš, 2002). Coupling ray theory proposed by Coates & Chapman (1990) provides a continuous transition between the isotropic and anisotropic ray theories and solves the problematic behaviour of S wave polarizations in inhomogeneous weakly anisotropic velocity models. The coupling ray theory provides more accurate polarizations and travel times of S waves in inhomogeneous weakly anisotropic models than the anisotropic ray theory. There are many more or less accurate approximations of the coupling ray theory.

We test the application of the prevailing-frequency approximation of the coupling ray theory (Klimeš & Bulant, 2016) to 3-D ray-based Kirchhoff pre-stack depth scalar migration and compute migrated sections in two simple velocity models composed of two layers separated by a curved interface. The upper layer is inhomogeneous, anisotropic and the bottom layer is homogeneous, isotropic. The first model has weak anisotropy (QI) and the second model has approximately four times stronger anisotropy (QI4).

Ray-theory software package ANRAY (Gajewski & Pšenčík, 1990) and packages MODEL, CRT, FORMS (Červený, Klimeš & Pšenčík, 1988; Bulant, 1996; Bucha & Bulant, 2022) do not offer the possibility to calculate coupling ray-theory S waves in models with interfaces. In order to compute recorded wave field in an inhomogeneous weakly anisotropic model with interface, we used the Fourier pseudospectral method (Tessmer, 1995). We apply scalar imaging for the complete wave field in a single-layer velocity model with the same anisotropy as in the upper layer of the velocity model used to calculate the recorded wave field. Under the scalar migration, we understand the migration of just a single component of the complete recorded elastic wave field. For migration we utilize the MODEL, CRT, FORMS and DATA software packages (Červený, Klimeš & Pšenčík 1988; Bulant 1996; Bucha & Bulant 2022).

We migrate reflected PP, converted PS1 and PS2 elementary waves without the separation of the recorded complete wave field into P and S waves. For migration of the S-wave part we use the prevailing-frequency approximation of the coupling ray theory and for comparison we apply the anisotropic-ray-theory approximation. The differences in migrated images due to different S wave polarizations between the coupling ray theory and anisotropic ray theory are visible. Calculations using the prevailing-frequency approximation of the coupling ray theory are without problems in both models. On the other hand, for the anisotropic-ray-theory approximation in the model with weaker anisotropy (QI), we have to use limitation of Green function maxima, otherwise the migrated sections are wrong.

In spite of complex recorded wave fields, without decomposition, the migrated interfaces for the vertical component of the PP reflected wave, radial and transversal components of PS1 and PS2 converted waves are relatively good in all stacked migrated sections, with exception of spurious interface images close to the correct ones (please see two examples in Figures 1 and 2).

Acknowledgments

The author thanks Ekkehart Tessmer for providing the Fourier method code. The author also thanks Luděk Klimeš and Ivan Pšenčík for their help.

The research has been supported by the Czech Science Foundation under Contract 20-06887S and by the members of the consortium “Seismic Waves in Complex 3-D Structures” (see “<http://sw3d.cz>”).

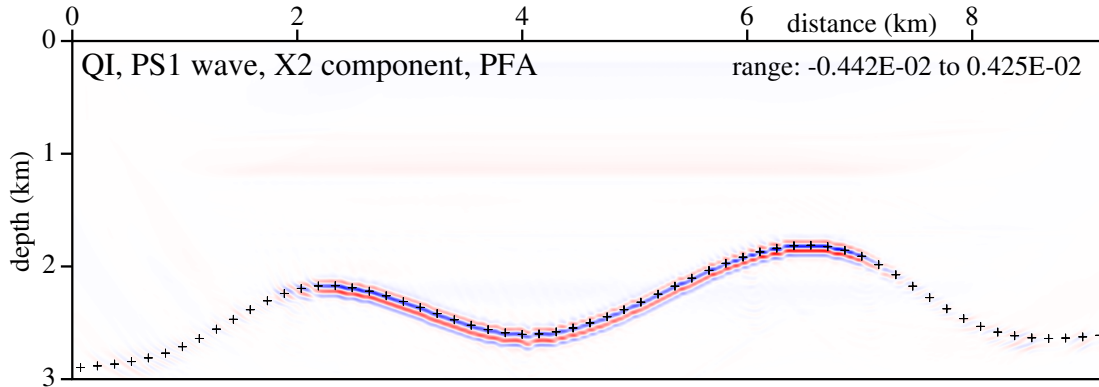


Figure 1. Stacked section migrated in the weakly anisotropic velocity model QI without interface. The transversal (X2) component of the PS1 converted wave is considered. Prevailing-frequency approximation (PFA) is used for calculation of the S-wave part of the converted PS1 wave. The elastic moduli in the single-layer velocity model for migration are the same as in the upper layer of the velocity model used to calculate the recorded wave field. 81×240 common-shot prestack depth migrated sections, corresponding to 81 profile lines and 240 sources along each profile line, have been stacked. The crosses denote the interface in the velocity model used to compute the recorded wave field. The top image of the interface is correct, the false image is slightly shifted downwards.

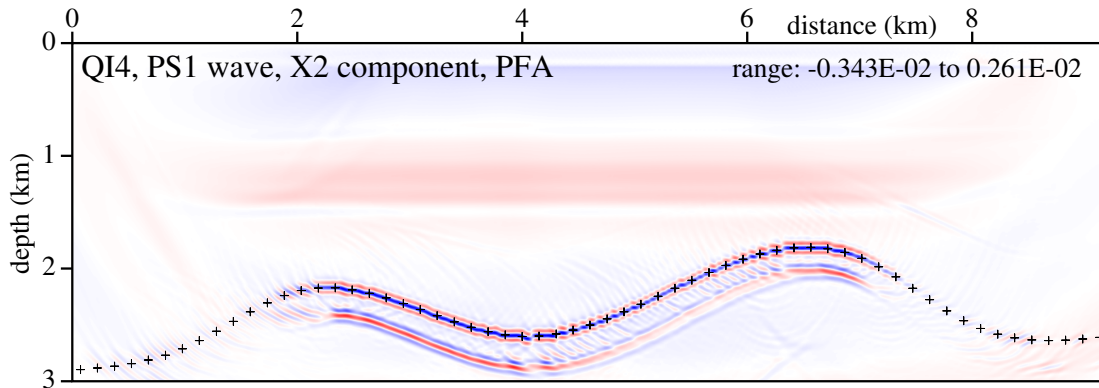


Figure 2. Stacked section migrated in the anisotropic velocity model QI4 without interface. The transversal (X2) component of the PS1 converted wave is considered. Prevailing-frequency approximation (PFA) is used for calculation of the S-wave part of the converted PS1 wave. The elastic moduli in the single-layer velocity model for migration are the same as in the upper layer of the velocity model used to calculate the recorded wave field. 81×240 common-shot prestack depth migrated sections, corresponding to 81 profile lines and 240 sources along each profile line, have been stacked. The crosses denote the interface in the velocity model used to compute the recorded wave field. The top image of the interface is correct, the false image is displaced downwards.

References

- Bucha, V. & Bulant, P. (eds.) (2022): SW3D-CD-25 (DVD-ROM). *Seismic Waves in Complex 3-D Structures*, **31**, 89–90, online at “<http://sw3d.cz>”.
- Bulant, P. (1996): Two-point ray tracing in 3-D. *Pure appl. Geophys.*, **148**, 421–447.
- Bulant, P. & Klimes, L. (2002): Numerical algorithm of the coupling ray theory in weakly anisotropic media. *Pure appl. Geophys.*, **159**, 1419–1435.
- Červený, V., Klimeš, L. & Pšenčík, I. (1988): Complete seismic-ray tracing in three-dimensional structures. In: Doornbos, D.J. (ed.), *Seismological Algorithms*, Academic Press, New York, pp. 89–168.
- Coates, R.T. & Chapman, C.H. (1990): Quasi-shear wave coupling in weakly anisotropic 3-D media. *Geophys. J. Int.*, **103**, 301–320.
- Gajewski, D. & Pšenčík, I. (1990): Vertical seismic profile synthetics by dynamic ray tracing in laterally varying layered anisotropic structures. *J. geophys. Res.*, **95B**, 11301–11315.
- Klimes, L. & Bulant, P. (2016): Prevailing-frequency approximation of the coupling ray theory for electromagnetic waves or elastic S waves. *Stud. geophys. geod.*, **60**, 419–450.
- Tessmer, E. (1995): 3-D seismic modeling of general material anisotropy in the presence of the free surface by a Chebychev spectral method. *Geophys. J. Int.*, **121**, 557–575.

Advances in inverse problems in anisotropic elasticity for high-frequency waves

Maarten V. de Hoop

Rice University

We present advances in the analysis of inverse problems associated with high-frequency wave propagation and scattering in models of anisotropic elasticity. First, in the linearized-about-“elliptic” case of tomography, we show the generic uniqueness and stability, up to natural obstructions, for the mixed-ray transform in three-dimensional compact simple Riemannian manifolds. (A general Riemannian metric corresponds with elliptic anisotropy.) Second, we employ Finsler geometry for qP and discuss two results: (i) The determination of a compact Finsler manifold from its boundary distance map; and (ii) A foliated and reversible Finsler manifold is determined by its broken scattering relation. Third, we will summarize consequences of elastic anisotropy through the lens of algebraic geometry shedding light on when the qP sheet of a slowness surface (determined by a Finsler metric) determines the entire stiffness tensor.

Joint research with J. Ilmavirta, M. Lassas, T. Saksala and A. Várilly-Alvarado.

SEISMIC ARRAY ANALYSIS FOR THE ROBUST OBSERVATION OF ANISOTROPY

Lou Parkes, Mark Chapman, Andrew Curtis

Array analysis (analysing and interpreting slowness domain power spectra of plane waves) has become established as a key tool in applied geophysics. The method is predominantly used in 2D, to analyse surface waves from uncontrolled sources. Early applications focussed on nuclear explosion monitoring, but more recently the applications have widened to include characterising other seismic sources and inferring detailed information of Earth properties beneath the array. Emphasis has moved from studying seismic sources to deriving velocity structure. Extensive efforts are typically made to compensate for resolution limitations which are dependent on the array size and shape.

Seismic anisotropy is known to be pervasive in the Earth, and there are great advantages in being able to estimate it from array analysis. Unfortunately, it can be hard to distinguish the anisotropy from the directional variation of the array response caused by directionally dependent arrays. Anisotropic effects are typically subtle and require good resolution for their detection.

We analyse the problem of measuring seismic anisotropy using directionally dependent arrays. We demonstrate that the slowness picking process in array analysis will always be subject to anisotropic resolution, with the degree of this anisotropy relating to the array geometry. We show that, combined with other unavoidable sources of bias in the analysis, this can result in artificial and inaccurate observations of anisotropy. We explore ways to make the analysis and interpretation more robust to these influences, expanding the scenarios in which anisotropy can be reliably observed from array data. This would allow smaller, more directionally dependent arrays and lower frequency sources to be used to observe anisotropy robustly.

We test the commonly used approach of inverting for the slowness of a single plane wave from a slowness domain power spectrum and repeating this for sources from different azimuths. We use the resultant slowness picks to then invert for anisotropic parameters, highlighting the difficulty of considering the anisotropic uncertainty in a robust manner. We look at how different types of noise can bias this methodology, particularly where the arrays are strongly directionally dependent.

We compare this to an approach where we deconvolve the array response in the slowness domain, stack the deconvolved spectra of sources at different azimuths and then invert for anisotropic parameters from the resultant slowness domain power spectrum. We look at how this can be more robust to common noise types such as high velocity noise (such as body waves).

Finally, we look at how parameterisation and Jacobians in the slowness domain (using polar and Cartesian coordinates) differently bias the inversions and affect the results. We suggest it can be beneficial to do the analysis in polar coordinates in order to align with the parameters of interest, while using cartesian Jacobians when summing over the slowness domain in order to keep the inversions robust.

An example of multi parameter finite frequency tomography

Ed Wright* (Shell Global Solution International, B.V.), Chris Haneveld (Former Shell Global Solution International, B.V.) and René-Édouard Plessix (Shell Global Solutions International, B.V.)

SUMMARY

Finite frequency methods are essential to correctly interact with velocity heterogeneities on the scale length smaller than the dominate Fresnel zone, and to provide more accurate anisotropic parameter estimation. Dynamical properties along a central ray are used to calculate 3D volume Fréchet kernels for finite frequency tomography (FFTom), where sensitivity to the background model is approximated via an orthorhombic Eikonal under the weak anisotropy condition. A synthetic example is shown comparing the travel time residual after inversion for an η anomaly between ray Fréchet kernels, and 3D volume Fréchet kernels, using either reflection, transmission or both branches. It is shown that FFTomo provides further reduction of the travel time residual, and better recovers the shape and magnitude of the η anomaly when compared to ray tomography. FFTomo has been tested on real data examples (not shown in this abstract).

INTRODUCTION

In recent years, due to the advancements in compute power, and the availability of broadband seismic data, finite difference techniques, such as full waveform inversion (FWI), have become standard modelling and inversion tools. Ray based techniques, however, still hold their attraction, due to their computational efficiency, and their applicability to using picked residuals in both the data and migration domain. However, due to the high frequency assumption, standard ray based techniques are inadequate in forward and inverse modelling of velocity heterogeneities smaller than the dominant Fresnel zone of the propagating wave. In this regime, finite frequency physics affects your wave propagation and arrival times (Spetzler, 2001).

Extensions to ray tracing to include finite frequency effects have been explored before, namely Fresnel zone ray tracing, (Cervený, 1992), and in tomography (Spetzler, 2004). These examples highlight the mathematical elegance of using the paraxial ray approximation to estimate the Fresnel zone around the central ray, and the importance of finite frequency effects in the inversion of sub-Fresnel zone size velocity heterogeneities.

In this abstract 3D volume Fréchet kernels for a finite frequency cross correlated travel time are calculated via the paraxial approximation along a dynamically traced ray, taking into account all reflections and transmissions (Dahlen, 2000a,b; Montelli, 2004). This method introduces finite frequency physics via a single scattering ap-

proximation. We also include include 3D Fréchet kernels for orthorhombic parameters calculated via a non-tilted orthorhombic Eikonal under the weak anisotropy condition, similar to (Tsvankin, 1997; Pšenčík and Farra, 2005).

We demonstrate the method on a simple synthetic attempting to recover an oval η anomaly. Fréchet calculations are done using both ray, and 3D Fréchet kernels, for transmission and reflection travel time branches. Comparisons are then made between the travel time residuals in the updated velocity models.

THEORY

Following the derivation given by (Dahlen, 2000a), the travel time perturbation, δT , can be written as,

$$\delta T = \int_V \left[\sum_i K_i \left(\delta m_i \frac{\partial G}{\partial m_i} \right) \right] dx dy dz, \quad (1)$$

where G is the Eikonal, and the sum is over all model sensitivity parameters, $m_i = [V_n, \delta, \delta_D, \eta, \eta_D, \eta_3, \chi]$. For example, the Fréchet kernel, K_η , is,

$$K_\eta = -\frac{1}{2\pi} F(\vec{x}, \vec{y}, \vec{z}, \omega, \Lambda) \frac{\delta \eta 2V_N^2}{1 + 2\delta} \left(A(1 + 2\delta) + 2B\delta_D - \frac{Ap_z^2}{\|\vec{p}\|^2} \right), \quad (2)$$

where F is the term containing the power spectrum, centered around the dominant frequency, ω , which is approximated by a first order derivative of a Gaussian (Favier, 2003). Λ is the geometrical spreading term calculated via the second order travel time Hessians along the central ray connecting the shot to receiver and receiver to shot respectively. The term F is calculated within the first dominant Fresnel zone. $A = p_x^2 + p_y^2$ and $B = (p_y^2 - p_x^2) \cos 2\chi + 2p_x p_y \sin 2\chi$. Here, V_N , is the normal moveout interval velocity, angle χ describes the orientation of the principal axes of symmetry in the horizontal plane, $\hat{p} = (p_x, p_y, p_z)$ defines the slowness vector, $\delta = 0.5(\delta_1 + \delta_2)$ represents Thomsen's transverse isotropy (TI) parameter (Thomsen, 1986), which is an average of Tsvankin's δ_1 and δ_2 parameters (Tsvankin, 1997), and $\delta_D = 0.5(\delta_1 - \delta_2)$ is a measure of the near offset azimuthal anisotropy. $\eta = 0.5(\eta_1 + \eta_2)$ is Alkhali-fah's anellipticity parameters (Alkhali-fah and Tsvankin, 1995), given as the average across the symmetry planes, as for δ_1, δ_2 . η_D is a measure of the far offset azimuthal anisotropy, and η_3 is the anellipticity in the horizontal plane. All velocity terms are spatially dependent. Note that tilt angles can be applied to model tilted orthorhombic media, but the tomography is restricted to the angle χ .

An example of multi parameter finite frequency tomography

Once the forward and inverse modelling is complete, a linear solve is performed in order to calculate the model parameter update. In order to stabilise the inversion, the second order derivative of the velocity update is also minimised, determined by a user defined smoothing parameter.

SYNTHETIC EXAMPLE

8[km] offset reflection and transmission travel time data is generated between a single shot and receiver located at $z = 0$ [km]. The reflection is from a horizontal reflector at $z = 3.5$ [km]. The travel time residual for each branch is calculated by subtracting the travel time in the background velocity, t_{bg} , where $v_{bg} = 2000[m s^{-1}] + 0.8z$, with the travel time in the background velocity model containing a smoothed ellipsoidal, η anomaly, t_{bg+eta} , which has a maximum η value of 0.2. The residuals were found to be, $dt_{bg}^t = -122.35[ms]$, for the transmission branch, t , and $dt_{bg}^r = -46.1[ms]$ for the reflection branch, r .

The results in figure 1 show example vertical cross sections comparing, (a), the interaction of η transmission and reflection Fréchet sensitivities for ray and, (b), the 3D Fréchet kernel from equation 1. The dominate frequency used to generate the η kernel has been chosen so the first Fresnel zone is roughly the same size as the anomaly, in this case $10Hz$. Starting with the background, bg , model, we attempt to recover the η anomaly via inversion, using the respective residuals for the separate branches.

The transmission only branch inversion reduced the travel time residual to $dt_{ray}^t = -29.47[ms]$ and $dt_{FFTomato}^t = -2.87[ms]$. The updated η profiles are shown in figure 1 (c) and (d) respectively. The reflection only branch inversion reduced the travel time residual to $dt_{ray}^r = -7.41[ms]$ and $dt_{FFTomato}^r = 7.68[ms]$. The updated η profiles are shown in figure 1 (e) and (f) respectively. Using both branches for the inversion reduced the travel time residual to $dt_{ray}^b = -18.97[ms]$ and $dt_{FFTomato}^b = -1.78[ms]$. The updated η profiles are shown in figure 1 (g) and (h) respectively.

Due to the horizontal propagation of the central ray, the diving wave is most sensitive to the changes in η , and this is reflected in both the updates for ray and FFTomo. However, due to the extra infill of the Jacobian from the 3D volume Fréchet integration, FFTomo shows both a significant decrease in the residual compared to ray only and better recovers the shape and magnitude of the η anomaly.

The smoothing parameters have been balanced to ensure the same smoothing is applied between a ray inversion, and an FFTomo inversion.

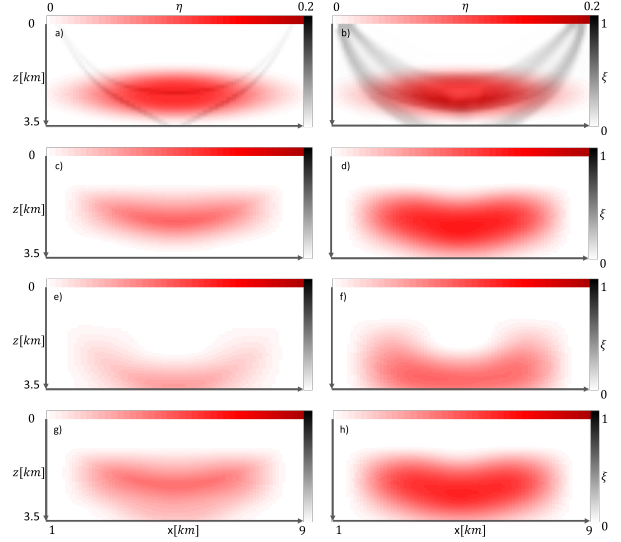


Figure 1: (a) Vertical cross section showing the interaction of transmission and reflection η sensitivity kernels, ξ , for rays due to an η anomaly (shown in red), which is embedded into a $v_0 + kz$ background vertical velocity profile. (b) Same vertical cross section, but FFTomo kernels are shown at $10Hz$. (c) Starting from an isotropic model, the inversion result for η using only the transmission ray kernel. (d) As (c), but an FFTomo transmission kernel is used. (e) As (c), but a ray reflection kernel is used. (f) As (c), but an FFTomo reflection kernel is used. (g) As (c), but both ray transmission and reflection kernels are used. (h) As (c), but both FFTomo transmission and reflection kernels are used.

DISCUSSION

An extension has been made to the ray based method to include a single scattering approximation allowing for finite frequency tomography with 3D Fréchet kernel sensitivities to orthorhombic parameters. In the synthetic example shown, due to the 3D volume Fréchet integration, FFTomo better recovers the shape and reduces the residual when compared to a ray approach. FFTomo offers an efficient and robust way to introduce finite frequency physics into the ray based work flow, while maintaining all the benefits of ray tracing. Future work will focus on combining FFTomo with finite difference techniques, and exploring frequency continuation work flows.

ACKNOWLEDGMENTS

I wish to thank the Advanced Imaging group for making this research possible, everyone in the **SMART** team, and Shell Global Solutions International, B.V.

An example of multi parameter finite frequency tomography

REFERENCES

- Alkhalifah, T., and I. Tsvankin, 1995, Velocity analysis for transversely isotropic media: *Geophysics*, **60**, 1550–1566.
- Cerveny, V., 1992, Fresnel volume ray tracing: *Geophysics*, **57**, 902–915.
- Dahlen, F., 2000a, Frechet kernels for finite-frequency traveltime - i. theory: *Geophys. J. Int.*, **141**, 157–174.
- , 2000b, Frechet kernels for finite-frequency traveltime - ii. examples: *Geophys. J. Int.*, **141**, 175–203.
- Favier, N., 2003, Sensitivity kernels for shear wave splitting in transverse isotropic media: *Geophys. J. Int.*, **153**, 213–228.
- Montelli, R., 2004, Global p and pp traveltime tomography: rays versus waves: *Geophys. J. Int.*, **158**, 637–654.
- Pšenčík, I., and V. Farra, 2005, First-order ray tracing for qP waves in inhomogeneous weakly anisotropic media: *Geophysics*, **70**, D65–D75.
- Spetzler, J., 2001, The effect of small-scale heterogeneity on the arrival time of waves: *Geophys. J. Int.*, **145**, 786–796.
- , 2004, Tutorial the fresnel volume and transmitted waves: *Geophysics*, **69**, 653–663.
- Thomsen, L., 1986, Weak elastic anisotropy: *Geophysics*, **51**, 1954–1966.
- Tsvankin, I., 1997, Anisotropic parameters and P-wave velocity for orthorhombic media: *Geophysics*, **62**, 1292–1309.

HUYGENS' PRINCIPLE AND DIFFRACTION - A COMPLEX HISTORY

T.J. Moser, Moser Geophysical Services, The Hague, The Netherlands
t.j.moser@mgeoph.com

The history of diffraction theory is a fascinating, entertaining and at times even anecdotal topic. The observations in real life that sound can be heard and light can be seen when the source is hidden, as well as the way water waves move around obstacles, have no doubt excited human imagination since the dawn of time. Experimental physics peaked in the 18th and 19th century when the “physique amusante” was a popular pastime. Optical and diffraction phenomena played a key role in these experiments.

We briefly review in historical order the key contributions to the development of the theory of diffraction. The work of Grimaldi, Huygens and Young provides the first part of this story, giving an understanding of diffraction and interference phenomena. Huygens, thanks to the principle which was named after him (indeed Huygens' principle), was able to explain the laws of reflection and refraction, but a deeper understanding of interference was still missing. This was provided by Young who used it to show how diffraction could arise from the interference of two waves. Fresnel, Helmholtz and Kirchhoff chose a different path and developed a full mathematical expression of Huygens' principle, incorporating wave phase and interference. Sommerfeld and his students were able to reformulate the Huygens-Helmholtz-Kirchhoff integral as the sum of an incident geometrical-optics wave and a diffraction integral, which is interpretable as the contribution of the diffracted rays from the boundary. A full ray-theoretical theory of diffraction, the Geometrical Theory of Diffraction, was given by Keller and extended by Klem-Musatov and Aizenberg to the case of seismic diffraction analysis.

Given the central role and success of Huygens' principle in explaining diffraction phenomena, it remains one the major mysteries of history of science, why Huygens himself never studied diffraction or even mentioned it. In this paper, we explore this mystery in some more detail and try to find some clues to a solution.

References

- Hoeber H.C., Klem-Musatov K.D., Moser T.J. and M.Pelissier 2010. Diffractions - A Historical Perspective, *EAGE Expanded Abstracts*, Barcelona.
- Hoeber H., Pelissier M., Moser T.J. and Klem-Musatov K. 2017. Seismic diffractions: How it all began, *First Break*, **35**, 31-34.
- Klem-Musatov K., Hoeber H.C., Moser T.J. and Pelissier M.A. (editors) 2016. *Classical and Modern Diffraction Theory*, Geophysical Reprint Series Nr 29, SEG.
- Klem-Musatov K., Hoeber H.C., Moser T.J. and Pelissier M.A. (editors) 2016. *Seismic Diffraction*, Geophysical Reprint Series Nr 30, SEG.

PREVAILING-FREQUENCY APPROXIMATION OF THE COUPLING RAY THEORY FOR S WAVES ALONG THE SH AND SV REFERENCE RAYS

Petr Bulant & Luděk Klimeš

*Department of Geophysics, Faculty of Mathematics and Physics, Charles University,
Ke Karlovu 3, 121 16 Praha 2, Czech Republic*

The coupling-ray-theory S-wave tensor Green function is frequency dependent. Its prevailing-frequency approximation removes this frequency dependence and allows us to introduce the coupling-ray-theory travel times and the coupling-ray-theory amplitudes, and to process the coupling-ray-theory wave field in the same way as the anisotropic-ray-theory wave field. This simplification may be decisive when storing the tensor Green function at the nodes of dense grids.

The coupling ray theory is usually applied to anisotropic common reference rays, but it is more accurate if it is applied to reference rays which are closer to the actual wave paths. In a generally anisotropic medium, the actual wave paths may be approximated by the anisotropic-ray-theory rays if these rays behave reasonably. In an approximately transversely isotropic medium, we can define and trace the SH and SV reference rays, and use them as reference rays for the prevailing-frequency approximation of the coupling ray theory.

We test the accuracy of the proposed prevailing-frequency approximation of the coupling ray theory numerically in the model with a split intersection singularity. The anisotropic-ray-theory S-wave rays crossing the split intersection singularity are smoothly but very sharply bent. While the initial-value rays can be safely traced by solving Hamilton's equations of rays, it is often impossible to determine the coefficients of the equations of geodesic deviation (paraxial ray equations, dynamic ray tracing equations) and to solve them numerically. As a result, we often know neither the matrix of geometrical spreading, nor the phase shift due to caustics. We demonstrate the abrupt changes of the geometrical spreading and wavefront curvature of the fast anisotropic-ray-theory S wave (Figure 1). We also demonstrate the formation of caustics and wavefront triplication of the slow anisotropic-ray-theory S wave (Figure 2).

Since the actual S waves propagate approximately along the SH and SV reference rays in this velocity model, we compare the anisotropic-ray-theory S-wave rays with the SH and SV reference rays (Figures 1 and 2). Since the coupling ray theory is usually calculated along the anisotropic common S-wave rays, we also compare the anisotropic common S-wave rays with the SH and SV reference rays.

Acknowledgements

The research has been supported by the Grant Agency of the Czech Republic under contract 20-06887S, and by the members of the consortium "Seismic Waves in Complex 3-D Structures" (see "<http://sw3d.cz>").

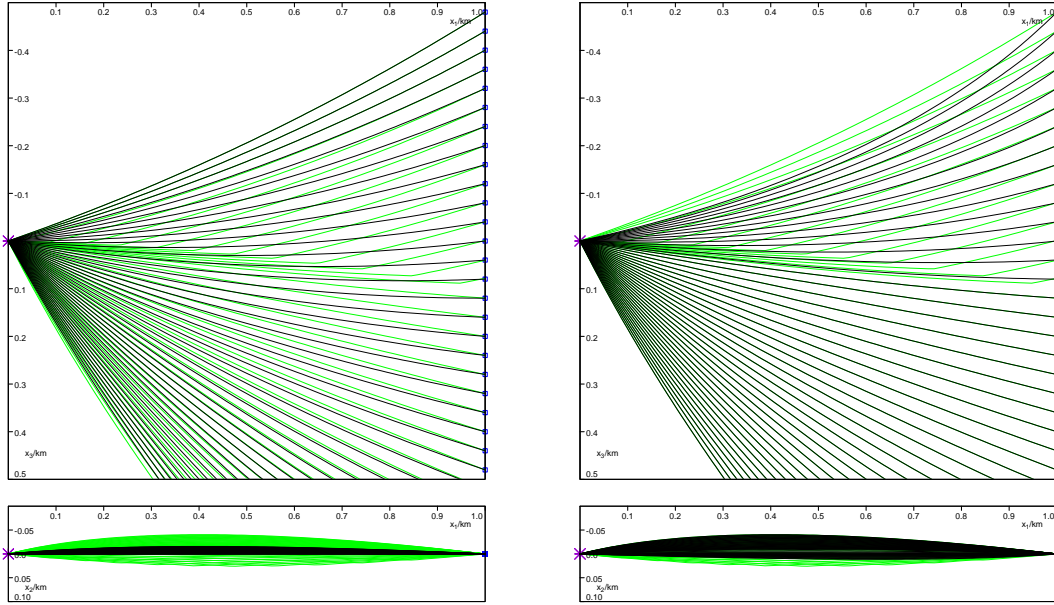


Figure 1: Left: Comparison of the anisotropic-ray-theory rays of the fast S wave (**green**) with the SH reference rays (**black**, plotted later on). The anisotropic-ray-theory rays of the fast S wave are very close to the SH reference rays for the deepest receivers, and are situated above them up to the third receiver below the surface. The anisotropic-ray-theory rays of the fast S wave are sharply bent from the second receiver below the surface to the ninth receiver above the surface, and considerably differ from the SH reference rays there. The anisotropic-ray-theory rays of the fast S wave nearly coincide with the SH reference rays from the tenth receiver above the surface.

Right: Comparison of the anisotropic-ray-theory rays of the fast S wave with the SV reference rays.

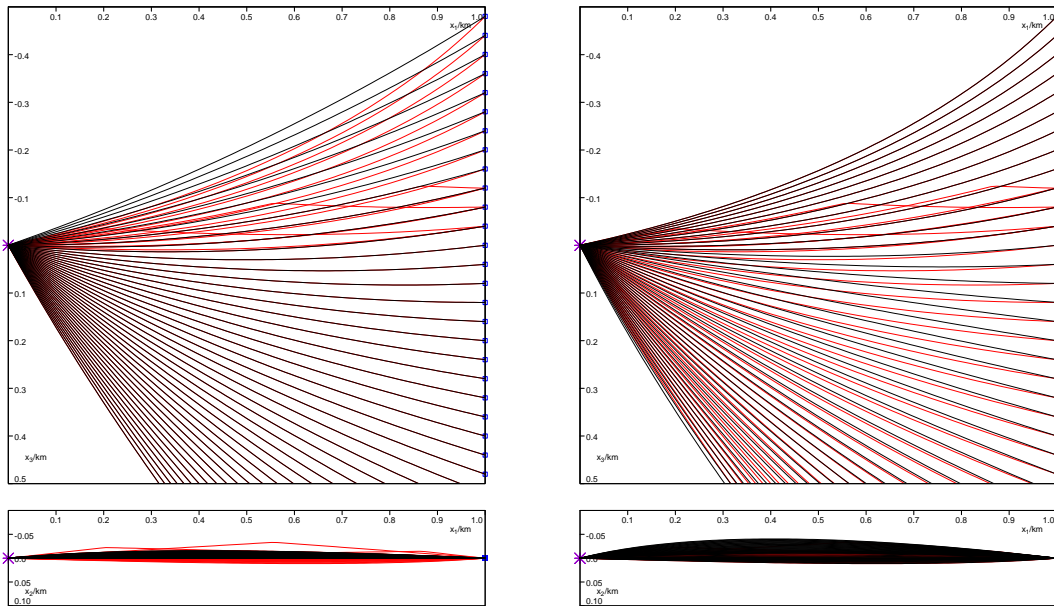


Figure 2: Left: Comparison of the anisotropic-ray-theory rays of the slow S wave (**red**) with the SH reference rays (**black**, plotted later on). The anisotropic-ray-theory rays of the slow S wave nearly coincide with the SH reference rays up to the surface receiver. The anisotropic-ray-theory rays of the slow S wave display a triplication due to sharply bent rays from the first to the third receiver above the surface. The anisotropic-ray-theory rays of the slow S wave are situated considerably below the SH reference rays from the fourth receiver above the surface.

Right: Comparison of the anisotropic-ray-theory rays of the slow S wave with the SV reference rays.

Diving waves in factorised orthorhombic media

Authors: Kristoffer Tesdal Galtung and Alexey Stovas

Introduction

Diving waves are very important for full wave inversion (FWI) applications. This is due to them being a major source of velocity information (Virieux and Operto, 2009; Plessix and Cao, 2011). By studying this type of wave using analytical models one can obtain much insight into how these behave for low-symmetry anisotropic models. Typically, this is done using factorized anisotropic (FAI) models. These are analytical models that have constant (or smoothly varying) anisotropic parameters and a linear variation of the vertical velocity with depth.

FAI models have been used to study wave propagation for special cases of orthorhombic anisotropy (isotropic, elliptical anisotropy, transverse isotropic anisotropy) (see. e.g., Stovas (2010), Stovas and Alkhalifah (2014) or Xu et al. (2016)). However, this is yet to be done for the general case of orthorhombic anisotropy. In this paper, we extend the FAI model for P-wave propagating in a low-symmetry anisotropic model, the factorized orthorhombic (ORT) model. To illustrate our method, we provide the comparison of penetration depth, relative geometrical spreading and ray trajectories for isotropic, elliptical and transversely isotropic models.

Factorized anisotropic models

To compute the properties of the linear velocity model (including the FAI models), we start with the equation for vertical slowness projection for P wave $p_3(p_1, p_2, z)$ computed for a given depth z , where p_1 and p_2 are the horizontal slowness projections. Then we compute the effective vertical slowness by taking the integral over the depth interval $(0, Z)$,

$$\tilde{p}_3(p_1, p_2, Z) = \frac{1}{Z} \int_0^Z p_3(p_1, p_2, z) dz, \quad (1)$$

taking into account that P wave vertical velocity is linearly varying with depth, $V = V_0 + Gz$, where V_0 is the velocity at zero depth and G is the velocity gradient. The penetration depth for the given p_1 and p_2 can be found from the solution of equation

$$p_3(p_1, p_2, Z) = 0. \quad (2)$$

Relative geometrical spreading

An important attribute of the diving waves is their amplitude. When analysing the seismic amplitudes, the geometrical spreading must be taken into account. Following Červený (2001), the formula for the relative geometrical spreading is given by

$$L = \Omega z \sqrt{|\det N|}, \quad (3)$$

where

$$\sqrt{|\det N|} = \sqrt{\left| \frac{\partial^2 \tilde{p}}{\partial p_1^2 \partial p_2^2} - \frac{\partial^2 \tilde{p}}{\partial p_1 \partial p_2} \frac{\partial^2 \tilde{p}}{\partial p_2 \partial p_1} \right|}, \quad \Omega = \cos \theta \quad (4)$$

In equation (4) θ is the take-off angle.

Anisotropic models

For the ORT model, the vertical slowness projection for this model is expressed as the following

$$p_3 = \frac{1}{V} \sqrt{\frac{1 - (a_1 p_1^2 + a_2 p_2^2) V^2 + a_{12} p_1^2 p_2^2 V^4}{1 - (b_1 p_1^2 + b_2 p_2^2) V^2 + b_{12} p_1^2 p_2^2 V^4}}, \quad (5)$$

where

$$\begin{aligned} a_1 &= (1+2\eta_1)(1+2\delta_1), a_2 = (1+2\eta_2)(1+2\delta_2), a_{12} = ((1+2\eta_1)(1+2\eta_2) - (1+2\eta_{xy})^2)(1+2\delta_1)(1+2\delta_2) \\ b_1 &= 2\eta_1(1+2\delta_1), b_2 = 2\eta_2(1+2\delta_2), b_{12} = 4(\eta_1\eta_2 - \eta_{xy}^2)(1+2\delta_1)(1+2\delta_2), \\ \eta_{xy} &= \frac{1}{2} \sqrt{\frac{(1+2\eta_1)(1+2\eta_2) - 1}{(1+2\eta_3)}}. \end{aligned} \quad (6)$$

Here η_1, η_2 and η_3 (we assume $\eta_j > 0$) are anelliptic parameters acting in all symmetry planes. The penetration depth (according to equation (2)) is given by

$$Z = \frac{1}{G} \left(\sqrt{\frac{2}{a_1 p_1^2 + a_2 p_2^2 + \sqrt{(a_1 p_1^2 + a_2 p_2^2)^2 - 4 a_{12} p_1^2 p_2^2}}} - V_0 \right) \quad (7)$$

We have to set the conditions, $a_1 a_2 > a_{12}$ and $a_{12} > 0$.

To obtain the penetration depth equations for the other types of mediums, the followings steps are taken to equation (3). For the isotropic medium: $a_1 = a_2 = 1, b_1 = b_2 = a_{12} = b_{12} = 0$, for the elliptical medium:

$a_1 = 1+2\delta_1, a_2 = 1+2\delta_2, b_1 = b_2 = a_{12} = b_{12} = 0$, and for the VTI medium: $a_1 = a_2 = (1+2\delta)(1+2\eta), b_1 = b_2 = 2\eta(1+2\delta), a_{12} = b_{12} = 0$.

Examples

We consider diving waves in different models with the same vertical velocity model ($V_0=2\text{ km/s}$ and $G=1\text{ km/s}$). The anisotropy parameters are set to 0 for the isotropic model, $\delta_1=0.1$, $\delta_2=-0.1$ for the elliptical model, $\delta=0$ and $\eta=0.2$ for the VTI model and $\eta_1=0.3$ and $\eta_2=\eta_3=0.1$ for the ORT model. Figures 1a and 1b accordingly show the penetration depths and the relative geometrical spreading at 1 km depth. Both figures are computed for models listed above for different values of horizontal slowness projections. The isoline shapes of these figures reflects the anisotropy of the model. The example of ray trajectories (for the same ray parameter) is illustrated in Figure 2. We can see that anisotropy plays a significant role in diving waves in factorized models.

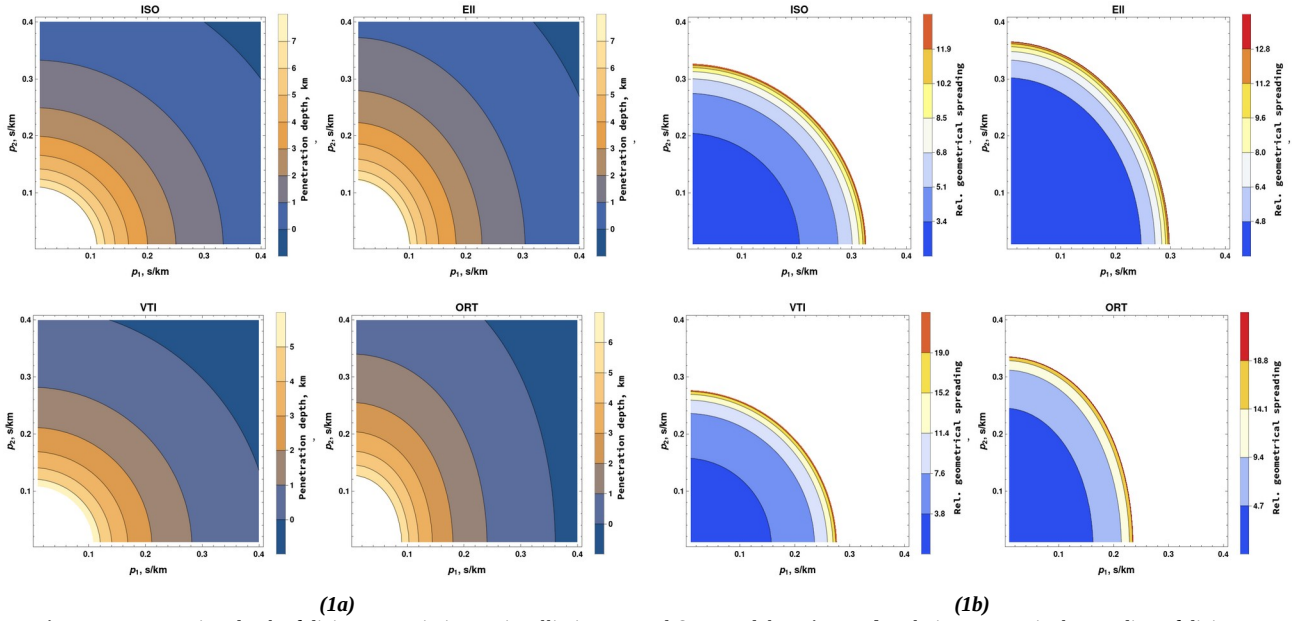


Figure 1a Penetration depth of diving waves in isotropic, elliptic, VTI and ORT models. **Figure 1b** Relative geometrical spreading of diving waves at 1 km depth in isotropic, elliptic, VTI and ORT models.

Conclusions

We derive equations for diving waves in anisotropic models and compare them in a numerical example. We also compute the penetration depth and relative geometrical spreading for the anisotropic models. The analytical ray tracing algorithm is illustrated for isotropic, elliptic, VTI and ORT models.

Acknowledgements

We would like to acknowledge CGF and GAMES at NTNU for financial support.

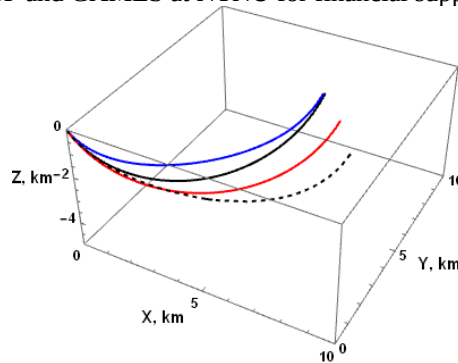


Figure 2 The ray trajectory of diving waves with $p_1=0.15\text{ s/km}$ and $p_2=0.14\text{ s/km}$ in isotropic (black solid line), elliptic (red solid line), VTI (blue solid line) and ORT (black dashed line) models.

References

- Červený, V. [2001] *Seismic ray theory*. Cambridge: Cambridge University Press.
- Plessix, R.-E., and Cao, Q [2011] A parametrization study for surface seismic full waveform inversion in an acoustic vertical transversely isotropic medium. *Geophysical Journal International*, 185, 539–556.
- Stovas, A [2010] Kinematical characteristics of the factorized velocity model. *Geophysical Prospecting*, 58, 219–227.
- Stovas, A. and Alkhalifah, T [2014] Analytical approximations of diving-wave imaging in constant gradient medium. *Geophysics*, 79, S131–S140.
- Virieux, J., and Operto, S [2009] An overview of full-waveform inversion in exploration geophysics. *Geophysics*, 74, no.6, WCC1–WCC26.
- Xu, S., Stovas, A. and Alkhalifah, T [2016] Estimation of the anisotropy parameters from imaging moveout in a factorized medium. *Geophysics* 81, no.4, C139–C150.

Slowness vector and ray velocity magnitude from ray direction in TTI media

Igor Ravve* and Zvi Koren, Emerson

Introduction

The magnitude of the ray (group) velocity v_{ray} of a given wave type vs. the ray direction \mathbf{r} , along with its spatial and directional derivatives, is required in many seismic-based applications in anisotropic elastic media, in particular, two-point ray-bending methods (e.g., Koren and Ravve, 2021), moveout approximations, seismic tomography, etc. This magnitude, in turn, depends on the components of the unknown slowness vector \mathbf{p} to be established, $v_{\text{ray}}^{-1} = \mathbf{p} \cdot \mathbf{r}$. For a given density-normalized fourth-order stiffness tensor of general anisotropy, $\tilde{\mathbf{C}}(\mathbf{x})$, a wave type and a ray direction vector \mathbf{r} , the resolving Hamiltonian-related equation set is,

$$H(\mathbf{x}, \mathbf{p}) = \det(\Gamma - \mathbf{I}) = 0, \quad \Gamma(\mathbf{x}, \mathbf{p}) = \mathbf{p} \tilde{\mathbf{C}}(\mathbf{x}) \mathbf{p}, \quad (1)$$

where $\Gamma(\mathbf{x}, \mathbf{p})$ is the Christoffel 3×3 tensor and \mathbf{I} is the identity matrix. For general (triclinic) anisotropy, this equation set consists of three polynomial equations: one of degree six and two of degree five. Grechka (2017) analyzed the algebraic complexity of the ray velocity surface and proved that the number of relevant real solutions does not exceed 19: a unique solution for the quasi-compressional wave, where the ray velocity surface is outward-convex, and up to 18 solutions for the quasi-shear waves. For polar anisotropy (TTI), Dellinger (1991) formulated the conditions for a triplication of qSV wavefronts, and Grechka (2013) demonstrated that there may be either one or three different solutions (due to triplications) for qSV slowness vectors vs. the given ray direction. We suggest a new approach to compute the slowness vectors (and the corresponding ray velocity magnitudes) for all wave modes in polar anisotropic media, including the triplications for qSV waves. This approach leads to a sixth-degree polynomial equation, whose coefficients depend on the medium properties and the ray angle between the ray velocity and the symmetry axis, while the roots are the phase angles between the slowness direction and the symmetry axis.

Governing Equation for Phase Angle

To compute the phase angles for the coupled qP and qSV waves, we first construct the Hamiltonian defined in equation 1 with the stiffness tensor of polar anisotropy and an arbitrary orientation of the medium symmetry axis. The first equation is the vanishing Hamiltonian. The collinearity condition of the slowness-related gradient of the Hamiltonian and the ray velocity direction \mathbf{r} leads to a vanishing cross-product, $\nabla_{\mathbf{p}} H \times \mathbf{r} = 0$, which in turn,

represents three linearly dependent Cartesian components of a vector equation. We exploit the fact that in TTI media the three vectors - ray velocity, slowness, and axis of symmetry - are coplanar. Thus, the slowness vector \mathbf{p} can be presented as a linear combination of the two known unit-length vectors: the axis of symmetry \mathbf{k} and the ray direction \mathbf{r} , with two unknown scalar coefficients. We introduce this linear combination in the collinearity condition, and the equation becomes a scalar bivariate polynomial of degree three. The other scalar equation is the vanishing Hamiltonian, and the inequality constraint about the positive projection of the slowness direction \mathbf{n} on the ray. Next, instead of searching for the two scalar coefficients of the slowness vectors, we introduce their ratio and reduce the set of two bivariate polynomial equations of degrees three and four, accompanied by the inequality constraint, to a single univariate polynomial equation of degree six,

$$d_6 c^6 + d_5 c^5 + d_4 c^4 + d_3 c^3 + d_2 c^2 + d_1 c + d_0 = 0, \quad (2)$$

where $c = \cot \vartheta_{\text{phs}}$. The coefficients of the polynomial read,

$$\begin{aligned} d_0 &= -(1+2\varepsilon)(1-f)(f+2\varepsilon)^2 m^2, \\ d_1 &= +2(f+2\varepsilon)^2 [1+\varepsilon-(1+\delta)f] m \sqrt{1-m^2}, \\ d_2 &= -4\varepsilon^2 (1-f) [1-(1+2f)m^2] - 2\varepsilon f \times \\ &\quad \left\{ 2(1-f) + (f+2\delta)f - [4-\delta(8-10f)-3(2-f)f] m^2 \right\} - f m^2 \times \\ &\quad \left\{ (1+2\delta)f(1-2\delta-f) + [f+8\delta-4(2-\delta)\delta f - (1-2\delta)f^2] \right\} \\ d_3 &= -\left\{ 2(1+\varepsilon)(\varepsilon-2\delta) - [1+3\varepsilon-2\delta(2+\delta)]f + (1+\varepsilon)f^2 \right\} \\ &\quad 4f m \sqrt{1-m^2}, \\ d_4 &= -2(1-f)f [2(2\delta-\varepsilon)+f] - f m^2 \times \\ &\quad \left\{ 2\varepsilon(2-f) - (4\delta^2+1-f)f - 2\delta [4-2(2+\varepsilon)f+f^2] \right\}, \\ d_5 &= +2f^2 [1+\varepsilon-(1+\delta)f] m \sqrt{1-m^2}, \\ d_6 &= -(1-f)f^2 (1-m^2), \quad f = 1 - v_S^2 / v_P^2, \quad m = \cos \vartheta_{\text{ray}} \end{aligned} \quad (3)$$

where ε and δ are the Thomsen (1986) parameters, and v_P, v_S are the axial compressional and shear velocities.

Numerical Example

Consider a polar anisotropic medium with the properties suggested by Grechka (2013), $v_P = 3 \text{ km/s}$, $f = 0.75$, $\delta = 0.3, \varepsilon = -0.15$. In Figures 1a and 1b, we plot the magnitudes of the phase (blue line) and the ray (orange line) velocities of the qP and SH waves, respectively. In Figures 1c and 1d we plot the magnitudes of the phase and ray velocities, respectively, of the triplicated qSV wave.

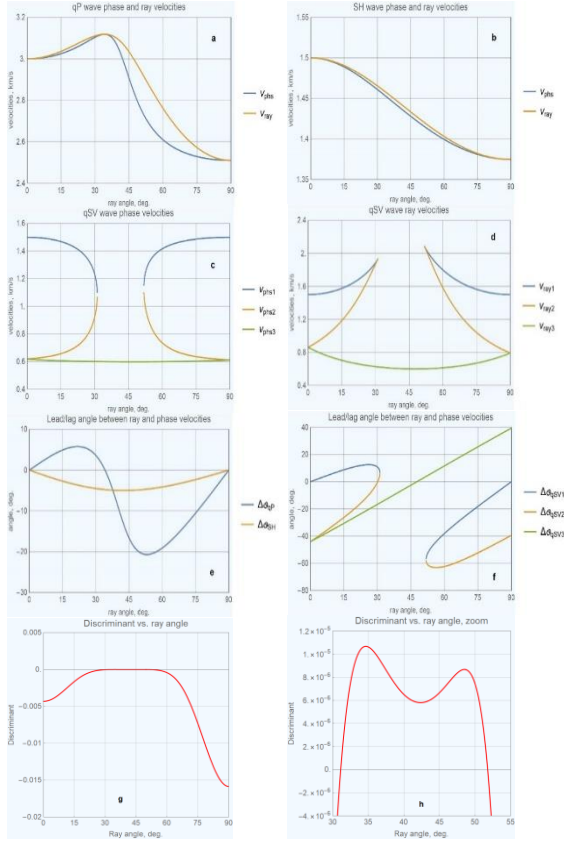


Figure 1: Characteristics of a TTI model vs. the ray angle between the axis of symmetry and the ray direction: a) phase and ray velocity magnitudes for the qP wave; b) phase and ray velocity magnitudes for the SH wave; c) phase velocity magnitudes for the triplicated qSV wave; d) ray velocity magnitudes for the triplicated qSV wave; e) lead/lag angles between the ray and phase velocity directions vs. ray angle for qP and SH waves; f) lead/lag angles between the ray and phase velocity directions vs. ray angle for the triplicated qSV wave; g) discriminant of the governing polynomial vs. the ray angle; h) discriminant of the governing polynomial, zoom in.

As can be seen in Figures 1c and 1d, at ray angles zero and 90° , the expected magnitudes of both qSV phase and ray velocities are present. The ray and phase velocities of this wave are shown by blue lines. However, due to the triplication, there are also two other qSV waves, with much lower phase and ray velocities shown by orange and green lines, respectively. The phase and ray velocities of the “orange” and “green” qSV waves coincide at the ends of the interval (ray angles zero and 90°) but differ elsewhere. In the proximity of 45° , there is no triplication: only the “green” qSV wave exists. In Figure 1e, we plot the signed lead/lag angle between the ray and phase velocity directions of the qP (blue line) and SH (orange line) waves,

respectively. For the given model, this angle is always negative or zero for the SH wave and alternates in sign for the qP wave. In Figure 1f, we plot the lead/lag for the triplicated qSV wave. At both ends of the interval, the lag of the “blue” qSV wave is zero. This is a “regular” qSV wave, with both ray and phase velocity directions along the medium symmetry axis, or both in the isotropic plane (with identical azimuths). The absolute value of this angle defines the deviation of the phase velocity direction from the medium axis of symmetry (which is large in this example), but the phase azimuth remains undetermined. In Figure 1g we plot the discriminant of the governing sixth-order polynomial vs. the ray angle. Within the range $30^\circ \lesssim \vartheta_{\text{ray}} \lesssim 55^\circ$, the discriminant is close to zero, and we zoom in to show its sign in Figure 1h.

Conclusions

Considering elastic media characterized by polar anisotropy (TTI), we suggest a new method for computing the slowness vectors and corresponding ray velocity magnitudes, given the medium properties, the orientation of the symmetry axis, and the ray velocity direction. This kind of inversion is inherent in the solution of two-point ray bending problems. For the coupled qP and qSV waves, we show that the solutions can be obtained by finding the roots of a single univariate polynomial equation of degree six, whose coefficients depend on the medium properties and the ray angle, where the unknown parameter is the non-unique phase angle between the slowness vector and the symmetry axis. The six roots include a unique solution for qP waves and one or three solutions for qSV waves (depending on the existing or non-existing triplication). In addition, there are one or two pairs of complex-conjugate roots. One pair of complex-conjugate roots always exists and has a “cuspidal” nature. The second pair exists only in the absence of a qSV triplication. We provide a direct indication for the existence of a qSV triplication without the need to solve the polynomial equation.

References

- Grechka, V., 2013. Ray-direction velocities in VTI media, *Geophysics*, **78**, no. 1, F1-F5.
- Grechka, V., 2017. Algebraic degree of a general group-velocity surface, *Geophysics*, **82**, no. 4, WA45-WA53.
- Dellinger, J., 1991. Anisotropic seismic wave propagation, PhD Thesis, Stanford University, Stanford, CA, USA (<http://sepwww.stanford.edu/theses/sep69/>).
- Koren, Z. and I. Ravve, 2020. Eigenrays in 3D heterogeneous anisotropic media: Part I - Kinematics, Variational formulation, arXiv:2003.09406.
- Thomsen, L., 1986. Weak elastic anisotropy, *Geophysics*, **51**, no. 10, 1954–1966.

On Richards' paradox

Bjørn Ursin¹ and Lasse Amundsen²

¹*The Norwegian University of Science and Technology, Department of Electronic Systems, Acoustics Group, Trondheim, Norway. E-mail: bjorn.ursin@ntnu.no*

²*Equinor Research Centre, Trondheim, Norway, and The Norwegian University of Science and Technology, Department of Geoscience and Petroleum, Trondheim, Norway*

ABSTRACT

Richards (1984) showed that for plane waves in anelastic media there may be wave solutions which violate the radiation condition by having an increasing amplitude in the propagation direction. A plane wave must satisfy the dispersion relation (the wave equation) between the complex horizontal and vertical slownesses and the inverse of the complex wave speed squared. In order to satisfy the radiation condition the real and imaginary parts of each slowness must have the same sign. When this is not the case, the solution is a non-physical wave which violates the radiation condition (Ursin and Amundsen, 2022).

When the horizontal slowness is real this cannot occur.

The complete reflection response for an SH-wave from a horizontal interface separating two homogeneous media is given by an integral where the integration variable is the real horizontal slowness. The saddle-point or steepest descent method gives an approximation corresponding to complex rays where both slownesses are complex. The incoming and reflected plane waves are both homogeneous where the propagation direction and attenuation direction are parallel. The plane wave in the other medium must satisfy Snell's law and a new dispersion relation. Krebes and Daley (2007) showed that this wave may violate the radiation condition resulting in errors in the reflection coefficient for the reflected wave. Ursin et al. (2017) solved this problem by approximating the plane-wave integral with the method of stationary phase with a real horizontal slowness. They showed that the stationary-phase solution is close to a numerical simulation of the reflected wavefield. This shows that using complex rays may lead to non-physical wave solutions.

REFERENCES

Krebes, E.S. & Daley, P.F., 2007. Difficulties with computing anelastic plane-wave reflection and transmission coefficients, *Geophys. J. Int.*, 170, 205–216.

Richards, P.G., 1984. On wavefronts and interfaces in anelastic media, *Bull. seism. Soc. Am.*, 74, 2157–2165.

Ursin, B., Carcione, J. M., and Gei, D., 2017, A physical solution for plane SH waves in anelastic media. *Geophys. J. Internat.*, 209(2), 661-671.

Ursin, B., & Amundsen, L., 2022, Plane waves in anelastic media, *Geophys. J. Int.*, submitted.

UPDATE OF DIFFRACTION IMAGING AND MODELING - METHODS AND APPLICATIONS

T.J. Moser, Moser Geophysical Services, The Hague, The Netherlands
t.j.moser@mgeoph.com

Diffraction is the disruption of a wave propagating around and beyond an obstacle. It plays a role in many branches of science, for instance electromagnetic, optical, acoustical and water wave propagation, and has been a topic of scientific investigation for many centuries. Diffraction occurs in seismic wave propagation too, whenever the medium contains structural discontinuities. However, seismic processing and imaging have traditionally been focused on the reflection method, regarding diffracted events as noise.

Over the past twenty years a vast amount of publications has appeared devoted to methods for diffraction imaging. In the wake of these publications, diffraction imaging is becoming recognized as a technique for high-resolution imaging of small-scale structural details which - despite their small size – are essential for applications such as fracture detection, near-surface studies and hydrocarbon reservoir characterization, but which are usually overshadowed by standard processing/imaging geared towards reflections.

The basic principles of diffraction imaging are by now well established. Diffraction imaging aims at separating the diffraction content from the main wavefield and imaging it separately. This can be done by various approaches, in various domains (data- or image domain) and by making various levels of assumptions.

This paper focuses on applications of diffraction imaging and its customization to interpretation. Topics that will be covered include

- Diffraction imaging and Fresnel zone sampling – the diffraction and specular reflection components of the wavefield are related to different parts of the Fresnel zone and separating them out based on specularly allows to bring out different degrees of structural detail in the images.
- Structural and stratigraphic diffraction imaging - Structural diffraction imaging enhances the details of complex faulting at both fault block and reservoir scales. Stratigraphic diffraction imaging resolves the internal geometries of, e.g., channel systems.
- Diffraction imaging and well planning; because of its favorable properties in terms of resolution and illumination, diffraction imaging is well suited for the mapping and planning of borehole trajectories.
- Diffraction modeling has developed into a separate tool for interpretation and analysis of the diffraction response of small-scale structural features, and as a validation of the details seen in the diffraction image.

References

Pelissier M., Moser T.J., Yu C., Lang J., Sturzu I. And Popovici A.M. 2017. Interpretation value of diffractions and sub-specular reflections – applications on the Zhao Dong field, *First Break*, **35**, 61-68.

Bréthaut D., Hartstra B., Jaya M., Moser T.J., van Noort G. and Pelissier M. 2018. Improved prospect evaluation and drilling results in the Dutch North Sea with diffraction imaging, *First Break*, **36**, 33-39.

Grasmueck, M., Moser T.J., Pelissier M.A., Pajchel J. and Pomar K. 2015. Diffraction signatures of fracture intersections, *Interpretation*, **3**, SF55–SF68.

Moser T.J., Arntsen B., Johansen S., Raknes E.B. and Sangesland S. 2016. Seismic Diffraction Response from Boreholes, *EAGE Expanded Abstracts*, Vienna.

Moser T.J., Pelissier M.A., Yu C., Popovici A.M. and Sturzu I. 2016. Structural and stratigraphic diffraction-imaging applications on the Zhao Dong Field, Bohai Bay, China, *SEG Expanded Abstracts*, Dallas.

Moser T.J., Moskvil L.M., Angerer E., Kobusinski W., Pelissier M. and Orosz J. 2020. Diffraction imaging of the Wisting Discovery, 4th Naturally Fractured Reservoir Workshop, 11-13 February 2020, Ras Al Khaimah, United Arab Emirates.

Moser T.J., Pelissier M., Alai R., Hashim M.H.B., Nguyen N.H., Tang W.H., Khan F.A., Muhamad A.A.B., Slind C.L., Danial R.B. and Roslan R.B. 2020. Diffraction Imaging of Faults, Basement Fractures and Stratigraphy in the Southern Malay Basin, *EAGE Expanded Abstracts*, Amsterdam.

Podolak M., Kobusinski W., Moser T.J., Gierszewska D. and Solarski T. 2020. Diffraction Imaging in North-Western Poland, A 3D Land Seismic Case Study, *EAGE Expanded Abstracts*, Amsterdam.

Simultaneous estimation of microseismic source parameters and velocity model using a Gauss-Newton consistent scattering approach

Morten Jakobsen(1,3), Ujjwal Shekar(1,3), Kui Xiang(1) and Jakub W. Both(2,3),

(1)Department of Earth Science, (2)Department of Mathematics,
(3)VISTA Centre for Coupled Subsurface Dynamics, University of Bergen.

A complete characterization of a fluid-injection induced microseismic event includes determining the position, the source time function and the moment tensor [1]. This is a highly ill-posed inverse problem which generally requires some kind of regularization. For simplicity, we focus here on the development of a scalar wave equation based approach for determining the position of microseismic events [1-4], under the assumption that the other source parameters have been eliminated from the inverse problem, via the use of a source parameter isolation strategy [3] and/or source function independent full-waveform inversion (FWI) [4]. The microseismic imaging problem is still very challenging, since the determination of the position of a microseismic event requires an accurate seismic velocity model [5]. The construction of an accurate seismic velocity model from surface seismic data can in principle be done by full-waveform inversion [6-7]. However, surface seismic FWI often suffers from a lack of full illumination, especially if the velocity model includes salt bodies or other strongly scattering objects [5,6]. To improve the construction of the velocity model, one can in principle use microseismic events in connection with surface seismic FWI [5]. If there for example is a microseismic event below a salt body then this can be used for improved seismic FWI (sub-salt) imaging. The velocity model and event characterization problems are therefore strongly interconnected, in the sense that a good solution of the surface seismic FWI problem may help the microseismic FWI problem and vice-versa [5]. The standard approach to joint analysis of active seismic and passive microseismic waveform data is to process the two data sets sequentially. However, it is also possible to perform a more or less simultaneous inversion of active and passive seismic waveform data [5], either by using a simple gradient method or (preferably) a variant of Newton's method [5]. It has been suggested that the Gauss-Newton method is a good alternative to a simple gradient-based scheme for joint seismic and microseismic FWI. This is because the Gauss-Newton method accounts for approximate Hessian information that helps to mitigate the problem with cross-talk between perturbations in the source position and the seismic velocity model [5]. However, Newton-style inversion is relatively costly compared to the cost of the simpler gradient-based approaches, suggesting that reduction of computational cost is essential for further progress in this field.

In this study, we present a Gauss-Newton consistent scattering approach [6-7] for simultaneous inversion of surface seismic and sub-surface microseismic waveform data for the position of the microseismic event and the background velocity model. Our theory and method is formulated in the frequency domain and we make use of a limited number of frequencies in the inversion [6-7]. To perform efficient seismic wavefield modelling in the frequency domain, we first transform the Helmholtz equation into an equivalent integral equation of the Lippmann-Schwinger type [6-7], which is solved iteratively using a FFT-accelerated Krylov subspace method with a multi-grid pre-conditioner [8]. The computational cost is further reduced by creative use of a source-independent transition operator in connection with the iterative Gauss-Newton type inversion [6,9]. We illustrate the performance of our theory and method by inversion of synthetic surface seismic and sub-surface microseismic waveform data associated with a laterally inhomogeneous medium involving a salt body and a fault that leads to strong scattering and diffraction effects beyond the range of applicability for ray theory [2]. Our numerical results based on the scalar wave equation are encouraging. However, we have simplified the problem in several ways. Therefore, the talk will close with a presentation of some ideas related to the estimation of multiple source parameters in the presence of an anisotropic elastic background model [9].

References

- [1] Kim, Y., Liu, Q. And Tromp, J., 2011. Adjoint centroid-moment tensor inversions. *Geophys. J. Int.*, 186, 264-278.
- [2] Huang, C., Dong, L.G., Liu, Y.Z. and Yang, J., 2017. Acoustic wave-equation based full-waveform inversion microseismic source location using improved scattering-integral approach, *Geophys. J. Int.*, 209, 1476-1488.
- [3] Huang, C., Dong, L.G., Liu, Y.Z. and Yang, J.Z., 2017. Waveform-based source location method using a source parameter isolation strategy. *Geophysics*, 82, KS85-KS97.
- [4] Wang, H. and Alkhalifah, T., 2018. Microseismic imaging using a source function independent full-waveform inversion method. *Geophys. J. Int.*, 214, 46-57.
- [5] Igonin, N. And Innanen, K.A.. 2018. Analysis of simultaneous velocity and source parameter updates in microseismic FWI. SEG Annual Meeting, Expanded Abstract.
- [6] Jakobsen, M. and Wu, R.S., 2018. Accelerating the T-matrix approach to seismic full-waveform inversion by domain decomposition. *Geophysical Prospecting*, 66, 1039-1059.
- [7] Xiang, K., Jakobsen, M., Eikrem, K.S. and Nævdal, G., 2022. A matrix-free variant of the distorted Born iterative method for seismic full-waveform inversion, submitted.
- [8] Erlangga, Y.A., Oosterlee, C.W. and Vuik, C., A novel multigrid based preconditioner for heterogeneous Helmholtz problems. *SIAM J SCI Comput.*, 27, 1471-1492.
- [9] Jakobsen, M., Psencik, I., Iversen, E. And Ursin, B., 2020. Transition operator approach to seismic full-waveform inversion in arbitrary anisotropic elastic media. *Commun. Comput. Phys.*, 28, 297-327.

Anatomy of Mars SEIS data from deep learning

Maarten V. de Hoop

Joint research with R. Balestrieri, R. Baraniuk, S. Barkaoui, A. Bueno, M. Campillo, P. Lognonn\{e}, Seydoux, ..

We present a family of deep neural networks designed to perform polyphonic identification, classification, segmentation and forecasting tasks on streaming Mars SEIS data and, in parallel, on seismo-volcanic data on Earth. We follow unsupervised, supervised and active learning approaches. We refer to the architectures as deep scattering network, recurrent scattering network and variational recurrent scattering autoencoder; invoking a Bayesian network strategy, we obtain epistemic uncertainty and forecasting capabilities.

The seismic noise recorded by the InSight seismometer (SEIS) has been revealing numerous transient micro-events, associated mostly to an active Martian environment with wind bursts, pressure drops, in addition to thermally-induced cracks. Identifying these micro-events is critical for ensuring that none of these are wrongly classified as marsquake. With the mentioned architectures we first detect and cluster many micro-events in an unsupervised fashion, interpret these, and then identify and classify marsquakes with supervised and active learning.

FAST INTEGRAL EQUATION METHOD FOR MICRO-SEISMIC WAVEFORM MODELING

Ujjwal Shekhar¹, Morten Jakobsen¹, Einar Iversen¹, Inga Berre²

1. Department of Earth Science, 2. Department of Mathematics
University of Bergen

Abstract

The subsurface drilling activities has increased in the recent years. This can be attributed to the production of hydrocarbon, geothermal energy, ground water, sequestration of carbon-dioxide in the reservoir formation etc. Fluid injection/extraction affects the pore pressure within the rockmass and may also lead to reactivation of critically stressed pre-existing faults. In the case of fluid injection, pore pressure is increased and fracture failure is observed. When the fluid is extracted, crushing of the rock at depth due to compaction is witnessed. These mechanical breaking results from the change in the state of stress of a rockmass. This often leads to microseismic event. Microseismic events are very weak seismic events that can be detected by downhole or shallow-buried near surface sensors.

Aki and Richards (2002) gave mathematical expression for body force density in microseismic event in which they represented the source term as moment tensor. Several authors (Grechka, 2020; Michel and Tsvankin, 2017; Vavrycuk, 2007) have derived the expression for moment tensor components for the dislocation type source in anisotropic media. We want to demonstrate wave propagation due to the moment tensor source in elastic media. In the frequency domain, elastodynamic wave equation can be written as the two coupled integral equations (Jakobsen et al., 2020). The two coupled integral equations for the particle displacement and strain can be combined in a block matrix form that represents a vectorial integral equation of the Lippmann-Schwinger type. The integral equation approach is based on the decomposition of actual medium into a known reference medium and an unknown perturbation model. If the Green's functions for the reference model is known, it is only required to discretize the perturbation model. Discrete version of this equation can be written as a linear system in matrix form. Jakobsen et al. (2020) used a T-matrix based approach to solve the system of linear equations for the seismic forward modeling. Modeling of real seismic data through the implementation of matrix based methods involve high computational cost and memory consumption. We have utilized the Fourier transform technique to perform microseismic forward modeling efficiently, i.e. in a matrix free manner. Instead of using the direct solver, we solved the system of equations in an iterative way using the Krylov subspace method alongwith the implementation of fast Fourier transform to perform convolution of the Green's function or modified Green's function with the source term. In this way, the computational cost scales down from N^3 for matrix based method to $N \log N$ for matrix free method, where N is the number of grid points. The computational memory scales down from N^2 to N .

In the frequency domain, displacement field in background or reference medium can be given by elementwise multiplication of first order spatial derivative of the background Green's function in Fourier transformed coordinates with the moment tensor source term. The background strain field can be calculated in a similar way using the second order spatial derivative of the background Green's function. Firstly, the strain field in actual medium was calculated at every grid point using the Krylov subspace method. We tested the convergence of our scheme by plotting the relative residual error with iteration numbers and found that it minimizes to significantly low value in few iterations. Then we obtained the components of elastic displacement using the calculated strain field. This result can be used while performing frequency domain full waveform inversion for microseismic source location and moment tensor components.

References

- Aki, K. and P. G. Richards, 2002. Quantitative Seismology: University Science Books, Mill Valley, California.
- Grechka, V., 2020. Moment tensors of double-couple microseismic sources in anisotropic formations, *Geophysics* **85**(2), 1-43.
- Jakobsen, M., Psencik, I., Iversen, E., Ursin, B., 2020. Transition operator approach to seismic full-waveform inversion in arbitrary anisotropic elastic media., *Commun. Comput. Phys.*, **28**, 297-327.
- Michel, O.J. and Tsvankin, I., 2017. Waveform inversion for microseismic velocity analysis and event location in VTI media., *Geophysics*, No.4, WA95-WA103.
- Vavrycuk, V., 2007. On the retrieval of moment tensors from borehole data, *Geophysical Prospecting* **55**, no. 3, 381 - 391.

Induced supershear microseismic event with rupture directivity and superimposed attenuation effects

Miłosz Wcisło, František Staněk, František Gallovič, Shaojiang Wu and Ivan Pšenčík

We investigate combined rupture directivity and attenuation effects on direct waveforms of an induced microseismic event recorded in China. The event with $M_w \sim 1$ located at the depth of ~ 3800 m depth was recorded during the hydraulic fracturing of shale reservoir in North China, by a star-like surface array with 12 arms and a total of 1771 vertical component geophones, see Figure 1a. Rupture directivity is a fundamental effect that is well known for large natural earthquakes (Koketsu et al., 2016). Its observation in microseismic events is difficult due to usually insufficient station coverage and stronger effects of attenuation along wave propagation paths. Due to attenuation effects (described by global absorption factor t^*), amplitudes and frequency content of direct arrivals characterized by peak frequencies f_{peak} , that initially vary with direction, start to converge to similar values for the same offsets (Eisner et al., 2013).

From the dataset we selected 629 receivers (gray dots in Fig.1a) that provide clear symmetrical P-wave pulses with high signal-to-noise ratio that allowed reliable f_{peak} measurement. Measured f_{peak} shown in Figure 1b showed strong azimuthal pattern that was difficult to explain by variations of attenuation caused by differences in elevation of receivers with similar offsets. We suspected that the pattern could be caused by the rupture directivity. Using additional 98 amplitude picks (magenta dots in Fig. 1a), we computed ray-based Green's functions and performed full moment tensor inversion of P-wave arrival amplitudes. The analyzed event is of a strike-slip type with two nearly vertical nodal planes oriented in the NW-SE direction (strike: 326° , dip: 85° , rake: -180°) and in the NE-SW direction (strike: 236° , dip: 90° , rake: -5°), with the double couple (DC) component of 66%.

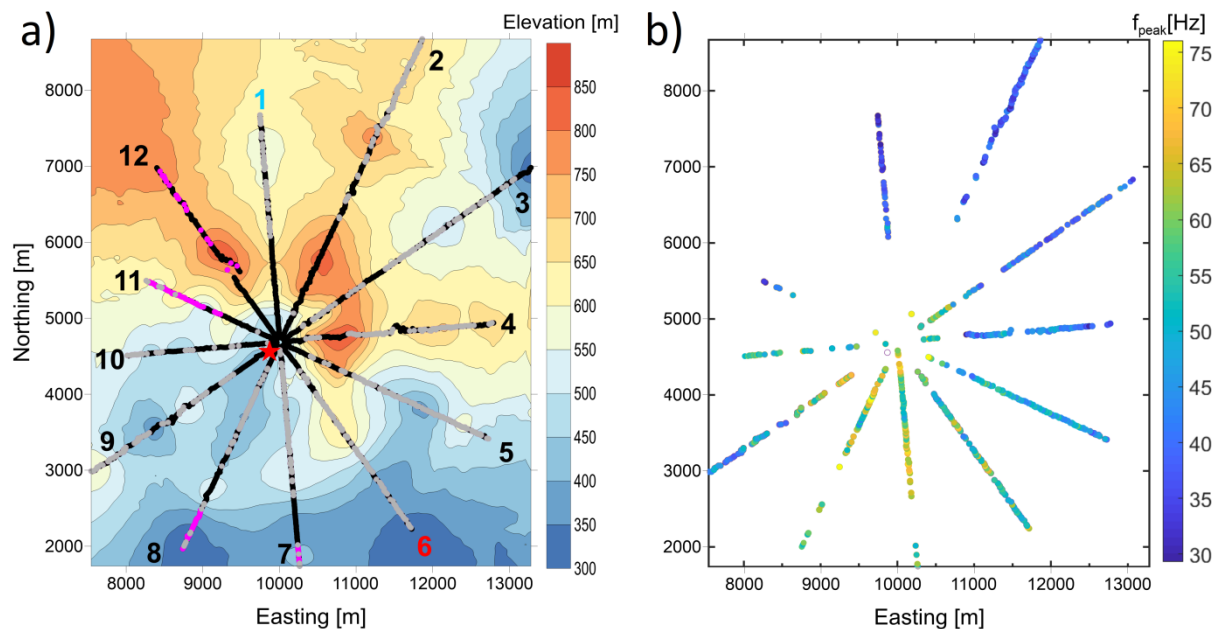


Figure 1. a) Map of the area of investigation including elevation. Dots show the positions of 1771 receivers that make up a star-like surface monitoring array with 12 arms. Receivers with clear, single P-wave arrival are in grey, receivers with additionally picked amplitude of P-wave arrival used in source mechanism inversion amplitudes are in magenta. The red star in the center represents the epicenter of the studied event. b) distribution of measured from direct arrivals peak frequencies.

We performed synthetic modelling of the peak frequencies for the investigated event at the receivers selected for peak frequency measurement locations. We grid searched for source rupture duration, rupture propagation direction, quality factor Q, and rupture velocity summarized in Table 1. The modelling provides better fit to measured f_{peak} from the data if rupture direction is included in the search than if the point source assumption (no directivity) is used. The best fit that explains broad range of measured f_{peak} is obtained if we allow the event to have supershear rupture propagation. Still, the highest values of the measured f_{peak} , which are found south to the event, are not fully explained by our modelling with single effective (average) Q in the whole area. The possible explanation of these high values is possible smaller thickness of the uppermost layer in the area – the elevation in this part of the array is lower. Near surface layer is usually the most attenuative. The modelling allowed us to choose the nodal plane of the event which is located in the NW-SE direction (strike: 326°, dip: 85°, rake: -180°).

		misfit	Q inverted	minimum / maximum synthetic f_{peak} value	range of observed f_{peak} explained (5 th -95 th percentile)
no directivity	constant peak frequencies	36,6	-	48 / 48	0%
	constant corner frequency (200hz)	18,1	150	37 / 53	49%
directivity	$V_{rupture}/V_S=0.9$	15,0	170	36 / 53	56%
	$V_{rupture}/V_S=1.5$	13,4	150	32 / 56	81%

Table 1. Summary of results of the modelling for 4 cases of different model complexity – from modelling that does not include attenuation and directivity effects, to the case, which includes attenuation and allows supershear rupture propagation. L2 misfit based on the differences of logarithms of measured and modelled f_{peak} is basis of misfit computation. Percentage of explained range of observed f_{peak} is computed using range from 5th to 95th percentile of observed in the data f_{peak} .

Acknowledgements

We thank the project Research Project 20-06887S of the Grant Agency of the Czech Republic, the project SVV 260581 of the Charles University, and the research project CzechGeo/EPOS LM2015079 of the Ministry of Education, Youth and Sports of the Czech Republic for support.

References:

- Eisner, L., Gei, D., Hallo, M., Opršal, I. Ali, M.Y., 2013. The peak frequency of direct waves for microseismic events, *Geophysics*. 78, A45-A49.
- Koketsu, K., Miyake, H., Guo, Y. et al., 2016. Widespread ground motion distribution caused by rupture directivity during the 2015 Gorkha, Nepal earthquake. *Scientific Reports*, 6, 28536.

Pore Pressure Mapping Using Microseismicity and Borehole Data.

Leo Eisner and Dmitry Alexandrov

The data describing the stress field normally includes either direct in-situ measurements in the wellbore, or indirect data – focal mechanisms of microearthquakes in the area of interest. Joint inversion of the source mechanisms and various types of borehole data allows recovering of both principal stress directions and magnitudes. A combination of data from reservoir injections and focal mechanisms from induced microseismicity allow reconstruction of the full stress tensor: stress orientation and principal stress magnitudes. Ultimately, the full stress tensor together with the focal mechanisms provide an estimate of pore pressure at the location of every event, which can be mapped in time and space. We successfully apply joint stress inversion to a Barnett shale hydraulic fracturing dataset and demonstrate pore pressure mapping.

Miłosz Wcisło, Ivan Pšenčík and José Carcione

The study of ray synthetic seismograms of reflected SH waves in attenuative media is a continuation of the work of Pšenčík et al. (2022) who applied the weak attenuation concept (WAC) to SH wave reflection/transmission (R/T) coefficients in the isotropic medium. The WAC is a perturbation technique, in which the attenuation is considered as a perturbation of the reference elastic state. Here we compare ray synthetic seismograms with WAC with full wave synthetic seismograms considered as an exact reference. The procedure is based on the Fourier and Chebyshev pseudospectral (PS) methods (Carcione, 2014).

For the tests, we use the seismograms of an SH wave reflected at an interface separating two homogeneous, isotropic elastic and anelastic half-spaces. The properties of the half-spaces (SH wave velocities, densities) are selected so that critical incidence in the reference elastic case is included, but Brewster angle is avoided in order to keep the models as simple as possible. The source and array of receivers are positioned at the same depth above the reflector. Dense step between receivers allows good mapping of the influence of the reflection coefficient on amplitude and phase of reflected waves. Three models of attenuation are used: the first model has both half-spaces elastic – this helps to evaluate general, not tied to the implementation of WAC, differences between ray and PS methods results. In the second model, first half-space is elastic and second anelastic. This model provides benchmark for the case where effects of attenuation are limited to the effects on the reflection coefficient. In the third model, both layers are anelastic, which allows to test the influence of the WAC during the propagation within the layer as well. As an example, the seismograms computed for the third model are shown in Figure 1. To facilitate comparison of results in each case, we computed maximum spectral amplitudes of computed seismograms. As an example, Figure 2 shows maximum spectral amplitudes for the model with both half-spaces anelastic.

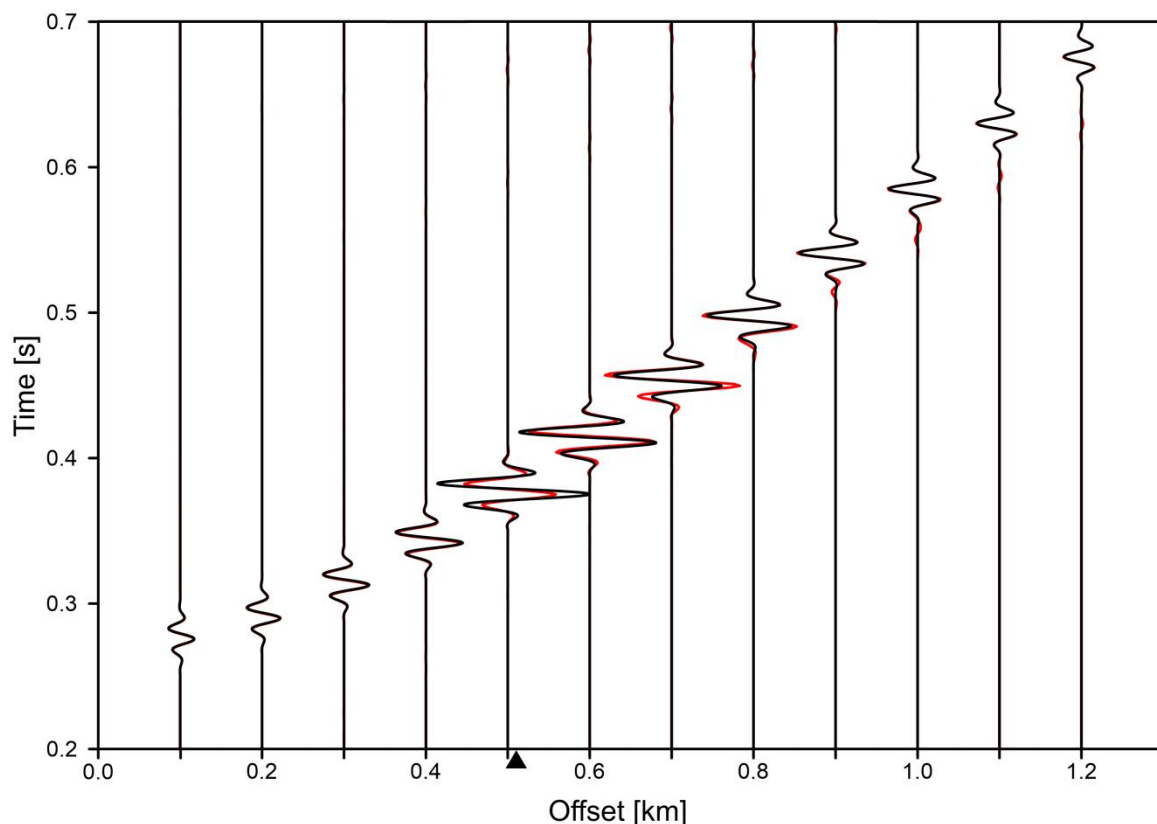


Figure 1: PS seismograms (red) overlaid by ray seismograms (black) in model with both half-spaces anelastic. Red arrival preceding the reflection behind the critical point (black triangle) is the head wave. Later red arrivals are numerical errors of the PS method.

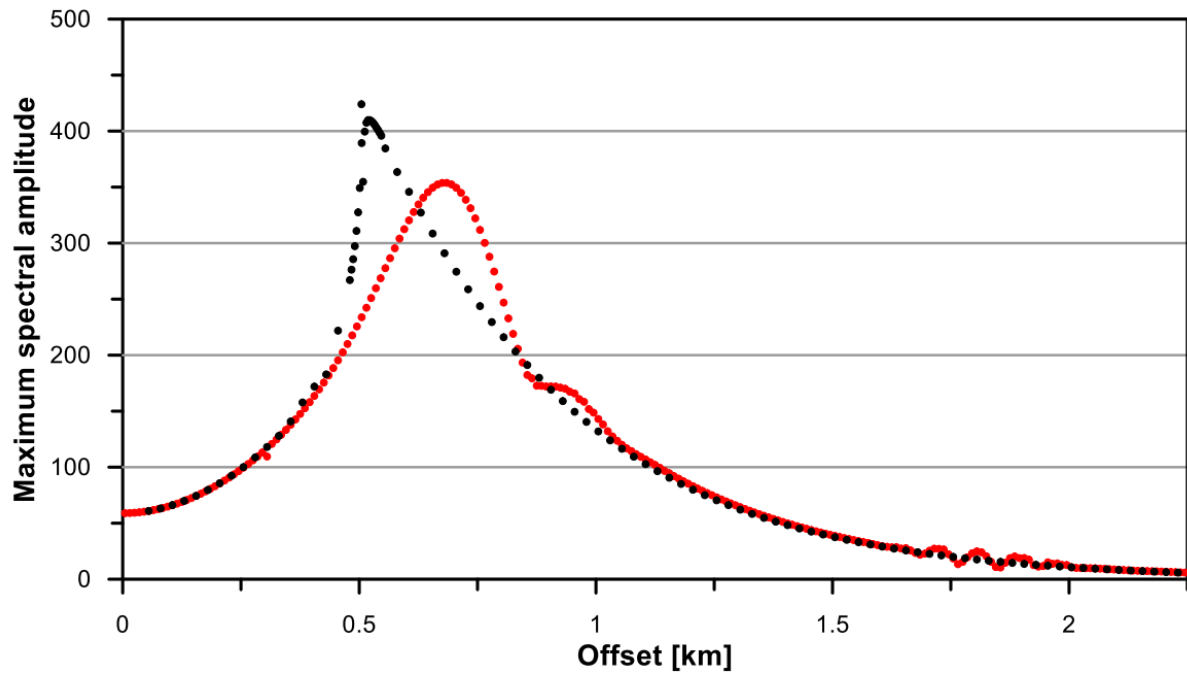


Figure 2: Maximum spectral amplitudes for model with both half-spaces anelastic calculated with the PS method (red) and by the ray method (black).

Results computed for the model with both half-spaces elastic show that outside the critical region ray results fit well the PS results. Differences in the critical region are caused by the ray method, which does not work properly in this region because it does not include head waves. Introduction of the attenuation effects on interface between half-spaces results in a small decrease of amplitudes in the vicinity of the critical angle for both methods. It does not increase the magnitude of differences between methods. Results computed for the model with both half-spaces anelastic, in which waves propagate inside attenuative layers, show that the decrease of amplitudes due to the attenuation effects at the interface are small in comparison to the decrease of amplitudes due to attenuation within the layers. Tests showed that outside the critical region the ray method with WAC yields results of satisfactory accuracy.

Acknowledgements

We thank the project Research Project 20-06887S of the Grant Agency of the Czech Republic, the project SVV 260581 of the Charles University, and the research project CzechGeo/EPOS LM2015079 of the Ministry of Education, Youth and Sports of the Czech Republic for support.

References:

Pšenčík, I., Wcisło, M., and Daley, P.F., 2022. SH plane-wave reflection/transmission coefficients in isotropic, weakly attenuating media. *Journal of Seismology*, doi.org/10.1007/s10950-021-10052-x.

Carcione, J. M., 2014. Wave fields in real media: wave propagation in anisotropic, anelastic, porous and electromagnetic media. In: *Handbook of Geophysical Exploration*, 3rd edn., revised and extended, Oxford.

THE DEGENERATE ELASTIC ORTHORHOMBIC MODELS

Alexey Stovas (NTNU, Norway), Yuriy Roganov (Tesseral, Ukraine) and Vyacheslav Roganov (Glushkov Institute, Ukraine)

Introduction

In low-symmetry anisotropy models, the singular directions (typically associated with S1 and S2 waves) are of importance due to complications in traveltimes, amplitudes and polarization fields in vicinity of these directions (Crampin, 1991). The singular directions result also in problems with application of perturbation methods in anisotropic media (Stovas et al., 2021b). The effect of singularity point in a very simple elliptical orthorhombic model (ORT) is shown in Stovas et al. (2021a). The detailed classification of ORT models based on the number and location of singular directions is given in Musgrave (1981). The classification of singularity points and analysis of their stability is described in Alshits et al. (1985). For general anisotropy, the analysis of singular directions is done by Vavryčuk (2005) and Roganov et al (2019). In our paper, we focus on singular directions in elastic orthorhombic model. For elastic orthorhombic model, we show that apart from the singularity points, we can also have the singularity line which is the feature of one-parameter family of degenerate ORT models. We analyze the conditions for degenerate ORT models and specify different classes of degeneracies.

Theory

First, we need to allocate the essential symmetry plane (Musgrave, 1981) from the magnitude of so-called “S waves stiffness coefficients” c_{44} , c_{55} and c_{66} . In our numerical example, we use the standard ORT model (Schoenberg and Helbig, 1997) with $c_{55} < c_{44} < c_{66}$, which results in 2-3 symmetry plane to be essential. The conditions for existence of singularity point in-between of symmetry planes of ORT model are given by setting the non-diagonal minors of Christoffel matrix to zero with three positive roots (Schoenberg and Helbig, 1997),

$$\begin{aligned} (c_{11} - f_{23})n_1^2 + c_{66}n_2^2 + c_{55}n_3^2 &= v_f^2, & c_{66}n_1^2 + (c_{22} - f_{13})n_2^2 + c_{44}n_3^2 &= v_f^2, \\ c_{55}n_1^2 + c_{44}n_2^2 + (c_{33} - f_{12})n_3^2 &= v_f^2, \end{aligned} \quad (1)$$

where n_j are the projections of the unit vector in phase domain, v_f^2 is the phase velocity squared for a singularity point, c_{jj} are the diagonal elements of the stiffness matrix and f_{kl} are the new variables given by

$$f_{12} = \frac{(c_{13} + c_{55})(c_{23} + c_{44})}{(c_{12} + c_{66})}, \quad f_{13} = \frac{(c_{12} + c_{66})(c_{23} + c_{44})}{(c_{13} + c_{55})}, \quad f_{23} = \frac{(c_{12} + c_{66})(c_{13} + c_{55})}{(c_{23} + c_{44})}. \quad (2)$$

We show, that if system of equations (1) is degenerate, we have a singularity line defined by intersection of the sphere and the cone, respectively given by equations,

$$n_1^2 + n_2^2 + n_3^2 = 1, \quad \frac{n_1^2}{v_f^2 - c_{44}} + \frac{n_2^2}{v_f^2 - c_{55}} + \frac{n_3^2}{v_f^2 - c_{66}} = 0. \quad (3)$$

We can distinguish between two cases depending on the value of v_f^2 : $c_{55} < v_f^2 < c_{44}$ (HTI-type) and $c_{44} < v_f^2 < c_{66}$ (VTI-type). Being projected to the horizontal symmetry plane, the singularity line is given by

$$\frac{(c_{66} - c_{44})n_1^2}{v_f^2 - c_{44}} + \frac{(c_{66} - c_{55})n_2^2}{v_f^2 - c_{55}} = 1, \quad (4)$$

which is either hyperbola (HTI-type) or ellipse (VTI-type). The non-diagonal stiffness coefficients for degenerate ORT model can be computed by using the value v_f^2 ,

$$\tilde{c}_{12}(v_f^2) = \sqrt{\tilde{f}_{13}\tilde{f}_{23}} - c_{66}, \quad \tilde{c}_{13}(v_f^2) = \sqrt{\tilde{f}_{12}\tilde{f}_{23}} - c_{55}, \quad \tilde{c}_{23}(v_f^2) = \sqrt{\tilde{f}_{12}\tilde{f}_{13}} - c_{44}, \quad (5)$$

where

$$\begin{aligned}\tilde{f}_{23} &= \frac{(c_{11}(v_f^2 - c_{44}) + c_{55}(c_{66} - v_f^2) - (c_{66} - c_{44})v_f^2)}{(v_f^2 - c_{44})}, \quad \tilde{f}_{13} = \frac{(c_{22}(v_f^2 - c_{55}) + c_{44}(c_{66} - v_f^2) - (c_{66} - c_{55})v_f^2)}{(v_f^2 - c_{55})}, \\ \tilde{f}_{12} &= \frac{(c_{33}(c_{66} - v_f^2) + c_{44}(v_f^2 - c_{55}) - (c_{66} - c_{55})v_f^2)}{(c_{66} - v_f^2)}.\end{aligned}\quad (6)$$

We can also define other combinations of v_f^2 -dependent stiffness coefficients, for example, $\tilde{c}_{11}(v_f^2)$, $\tilde{c}_{22}(v_f^2)$, $\tilde{c}_{33}(v_f^2)$. In case of degenerate ORT model, we have the singularity line connecting the essential and one of non-essential symmetry planes (depending on the type) and the singularity point located in this non-essential symmetry plane. In Figure, one can see the image of singularity line and singularity point in the group domain computed from the VTI-type degenerate ORT model with diagonal stiffness coefficients taken from the standard ORT model, but the non-diagonal coefficients computed from equations (5)-(6) with $v_f^2 = 2.05 \text{ km}^2/\text{s}^2$.

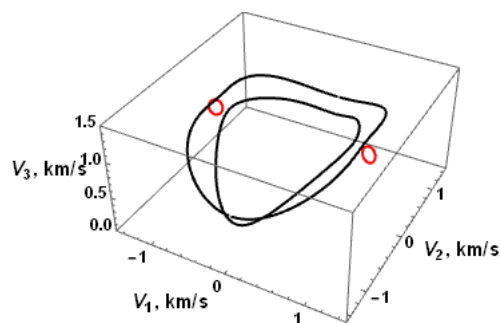


Figure. The image of the singularity line and the singularity point in group domain for degenerate ORT model with non-diagonal stiffness coefficients computed from equations (5)-(6) with $v_f^2 = 2.05 \text{ km}^2/\text{s}^2$.

Conclusions

We define the one-parameter family of degenerate ORT models resulting in a singularity line and a singularity point. Depending on the value of this parameter, the degenerate ORT model can be of HTI- and VTI-type. The image of singularity line and singularity point in the group domain is illustrated for the standard ORT model.

Acknowledgements

Alexey Stovas acknowledge the GAMES project for financial support.

References

- Alshits, V.I. Sarychev, A.V., and A.L. Shuvalov, 1985, Classification of degeneracies and analysis of their stability in the theory of elastic waves: *Zh. Eksp. Teor. Fiz.*, **89**, 922-938.
- Crampin, S., 1991, Effects of point singularities on shear-wave propagation in sedimentary basins: *Geophysical Journal International*, **107**, 531-543.
- Musgrave, M.J.P., 1981, On an elastodynamic classification of orthorhombic media: *Proc. R. Soc. London, Ser A*, **374**, 401-429.
- Roganov, Yu., Stovas, A., and V. Roganov, 2019, Properties of acoustic axes in triclinic media: *Geofizicheskiy zhurnal*, **41**, 3-17.
- Schoenberg, M., and K. Helbig, 1997, Orthorhombic media: Modeling elastic wave behavior in a vertically fractured earth: *Geophysics*, **62**, 1954-1974.
- Stovas, A., Roganov, Yu., and V. Roganov, 2021a, Wave characteristics in elliptical orthorhombic medium: *Geophysics*, **86**, C89-C99.
- Stovas, A., Roganov, Yu., and V. Roganov, 2021b, Perturbation of phase velocities in elastic orthorhombic media: *Geophysics*, **86**, C101-C118.
- Vavryčuk, V., 2005, Acoustic axes in triclinic anisotropy: *J. Acoust. Soc. Am.*, **118**, 647-653.

Seismic anisotropy of fractured shales

Leon Thomsen* and Colin Sayers, University of Houston

Summary

Explicit formulae are presented for anisotropic parameters for the orthorhombic case of a polar anisotropic body (for example a shale) penetrated by a single set of vertical, rotationally variant fractures (*e.g.* joints).

Fractured shales

Unfractured shales and thin-bed sequences are conveniently idealized as Polar Anisotropic formations. If such a formation is penetrated by a single set of vertical parallel fractures, the result is a special case of an orthorhombic medium wherein the elastic stiffness matrix C is given by Schoenberg and Helbig (1997), assuming that the vertical fractures have normals parallel to the 1-axis, as:

$$\begin{bmatrix} C_{11}^{PA} [1-\delta_N] & C_{12}^{PA} [1-\delta_N] & C_{13}^{PA} [1-\delta_N] & 0 & 0 & 0 \\ & C_{11}^{PA} [1-\delta_N g^2] & C_{13}^{PA} [1-\delta_N g] & 0 & 0 & 0 \\ & & C_{33}^{PA} [1-\delta_N h] & 0 & 0 & 0 \\ & & & C_{44}^{PA} & 0 & 0 \\ & & & & C_{44}^{PA} [1-\delta_V] & 0 \\ & & & & & C_{66}^{PA} [1-\delta_H] \end{bmatrix}$$

wherein only the upper triangle is shown. For flat-lying media, the 3-axis is vertical. The general expressions for the plane-wave velocities in orthorhombic media are quite complicated combinations of 9 independent parameters. But Miller and Spencer (1994), and Tsvankin (1997) noticed that, in the two principal vertical planes, they simplify without approximation to the expressions for Polar Anisotropic media (often confusingly referred to as “Vertically Transversely *Isotropic*” or “VTI” media). These latter expressions are well known (*e.g.* Thomsen, 1986), and are much simpler.

In the matrix C above, the moduli of the unfractured background Polar Anisotropic medium are denoted by $C_{\alpha\beta}^{PA}$. The non-dimensional fracture compliances δ_N , δ_V , and δ_H are related to the excess compliances Z_N , Z_V , and Z_H of the fracture set by

$$\delta_N \equiv \frac{Z_N C_{11}^{PA}}{1 + Z_N C_{11}^{PA}}; \quad \delta_V \equiv \frac{Z_V C_{44}^{PA}}{1 + Z_V C_{44}^{PA}}; \quad \delta_H \equiv \frac{Z_H C_{66}^{PA}}{1 + Z_H C_{66}^{PA}} \quad (1)$$

Here the subscripts N , V , H refer to Normal stresses (on the flat faces of the fractures), Vertical shear stresses, and Horizontal shear stresses, respectively. In the special case of rotationally invariant fractures (so-called “HTI” fractures), $Z_V = Z_H = Z_T$, but this assumption is physically unrealistic, especially for joints, which typically have lengths much

greater than their heights. Also shown above are scaling factors $g \equiv C_{12}^{PA} / C_{11}^{PA}$ and $h \equiv (C_{13}^{PA})^2 / C_{11}^{PA} C_{33}^{PA}$.

Note that here there are only 8 free parameters (5^{PA} parameters and 3 fracture parameters) represented among the 9 independent orthorhombic elements. Sayers (2022) discussed numerically a number of implications of these results of linear slip theory. Here we manipulate them algebraically to expose the anisotropy analytically.

Anisotropy parameters

In the case discussed here, the orthorhombic anisotropy parameters may be expressed in terms of the background anisotropy of the Polar Anisotropic medium and the compliances of the fractures. Assuming that the additional anisotropy caused by the fractures is small, but that the background anisotropy may be substantial, propagation in the 1-3 plane may be parametrized as:

$$V_{P0} \equiv \sqrt{\frac{C_{33}}{\rho}} \approx V_{P0}^{PA} \left(1 - \frac{\delta_N h}{2}\right); \quad V_{S0}^{13} \equiv \sqrt{\frac{C_{55}}{\rho}} \approx V_{S0}^{PA} \left(1 - \frac{\delta_V}{2}\right) \quad (2a)$$

$$\varepsilon_{13} \equiv \frac{C_{11} - C_{33}}{2C_{33}} \approx \varepsilon^{PA} (1 + \delta_N h) + \frac{\delta_N}{2} \left(h - \frac{C_{11}^{PA}}{C_{33}^{PA}} \right) \quad (2b)$$

$$\begin{aligned} \delta_{13} &\equiv \frac{(C_{13} + C_{55})^2 - (C_{33} - C_{55})^2}{2C_{33}(C_{33} - C_{55})} \\ &\approx \delta^{PA} \left[1 + \frac{\delta_N h (2C_{33}^{PA} - C_{55}^{PA}) - \delta_V C_{55}^{PA}}{(C_{33}^{PA} - C_{55}^{PA})} \right] + \end{aligned} \quad (2c)$$

$$\begin{aligned} &\delta_N h - \frac{\delta_N C_{13}^{PA} (C_{13}^{PA} + C_{55}^{PA}) + \delta_V C_{55}^{PA} (C_{13}^{PA} + C_{33}^{PA})}{C_{33}^{PA} (C_{33}^{PA} - C_{55}^{PA})} \\ \gamma_{13} &\equiv \frac{C_{66} - C_{55}}{2C_{55}} \approx \gamma^{PA} (1 + \delta_V - \delta_H) + \frac{\delta_V - \delta_H}{2} \end{aligned} \quad (2d)$$

where the parameters of the background PA medium are designated with a superscript ^{PA}.

If the background anisotropy δ^{PA} is weak, equation (2c) simplifies substantially:

$$\delta_{13} \approx \delta^{PA} + \delta_N h - \frac{(\delta_N C_{13}^{PA} + 2\delta_V C_{55}^{PA})}{C_{33}^{PA}} \quad (2e)$$

In the 2-3 plane:

$$V_{P0} \equiv \sqrt{\frac{C_{33}}{\rho}} \approx V_{P0}^{PA} \left(1 - \frac{\delta_N h}{2}\right); \quad V_{S0}^{23} \equiv \sqrt{\frac{C_{44}}{\rho}} = V_{S0}^{PA} \quad (3a)$$

$$\varepsilon_{23} \equiv \frac{C_{22} - C_{33}}{2C_{33}} \approx \varepsilon^{PA} (1 + \delta_N h) + \frac{\delta_N}{2} \left(h - \frac{g^2 C_{22}^{PA}}{C_{33}^{PA}} \right) \quad (3b)$$

$$\delta_{23} \equiv \frac{(C_{23} + C_{44})^2 - (C_{33} - C_{44})^2}{2C_{33}(C_{33} - C_{44})} \approx \delta^{PA} \left[1 + \delta_N h \frac{(2C_{33}^{PA} - C_{44}^{PA})}{(C_{33}^{PA} - C_{44}^{PA})} \right] + \delta_N h - \delta_N g \frac{C_{23}^{PA}(C_{23}^{PA} + C_{44}^{PA})}{C_{33}^{PA}(C_{33}^{PA} - C_{44}^{PA})} \quad (3c)$$

$$\gamma_{23} \equiv \frac{C_{66} - C_{44}}{2C_{44}} = \gamma^{PA} (1 - \delta_H) - \frac{\delta_H}{2} \quad (3d)$$

If the background anisotropy δ^{PA} is weak, equation (3c) simplifies substantially:

$$\delta_{23} \approx \delta^{PA} + \delta_N \left(h - g \frac{C_{23}^{PA}}{C_{33}^{PA}} \right) \quad (3e)$$

The 9th parameter may be taken as

$$\delta_{12} \equiv \frac{(C_{12} + C_{66})^2 - (C_{11} - C_{66})^2}{2C_{11}(C_{11} - C_{66})} \approx (2\delta_N - \delta_H) \frac{C_{66}^{PA}}{C_{11}^{PA}} \quad (4)$$

Notice that in the anisotropies $\varepsilon_{\alpha\beta}$ and $\delta_{\alpha\beta}$ for the two principal planes, equations (2,3), the fracture compliances which appear are δ_N and δ_V . The third fracture compliance δ_H only appears in the “9th” parameter δ_{12} , *cf.* Eq. (4), and in the shear parameters $\gamma_{\alpha\beta}$. This means that, in a P-wave problem, the difference between δ_H and δ_V is apparent between the principal planes, but not along them.

In these expressions for the anisotropy parameters, the most important are equations (2ce, 3ce), for the δ -parameters in the principal planes. These affect the short-spread P-wave moveout velocities in those planes (Tsvankin, 1997). Even more important are the consequences for AVO of these δ -anisotropies. Of course, the (normal-incidence) reflectivity intercepts must be the same in both principal planes. The reflectivity gradient (*i.e.*, the coefficient in the linearized plane-wave reflectivity of the $\sin^2\theta$ term, where θ is the angle of incidence) in each of the two planes is given (*e.g.* Lin and Thomsen, 2013) by

$$R_2^{13} = \frac{1}{2} \left[\frac{\Delta V_{P0}}{\bar{V}_{P0}} - \left(\frac{2\bar{V}_{S0}^{13}}{\bar{V}_{P0}} \right)^2 \frac{\Delta C_{55}^{PA}}{\bar{C}_{55}^{PA}} + \Delta\delta_{13} \right] \quad (5a)$$

$$R_2^{23} = \frac{1}{2} \left[\frac{\Delta V_{P0}}{\bar{V}_{P0}} - \left(\frac{2\bar{V}_{S0}^{23}}{\bar{V}_{P0}} \right)^2 \frac{\Delta C_{44}^{PA}}{\bar{C}_{44}^{PA}} + \Delta\delta_{23} \right] \quad (5b)$$

Here Δ indicates a jump across a reflecting interface, and the overbar indicates the average across the interface. If the formation on the other side of the reflecting horizon is isotropic, the jumps $\Delta\delta_{\alpha\beta}$ are given by the parameters $\delta_{\alpha\beta}$ directly, with an algebraic sign which depends upon whether the reflection is from the top or the bottom of the anisotropic bed.

The differences in the second term of (5ab) make marginal changes in the two gradients. But the last term $\Delta\delta_{\alpha\beta}$ in each of Eqs. (5a,b), although assumed to be small compared to

one, is not necessarily small compared to the other terms in the expression, which are all assumed to be small compared to one. Hence it may make a significant contribution to the AVO gradient, even though it is much less than one.

Each of these terms $\Delta\delta_{\alpha\beta}$ contain (*cf.* equations (2e,3e)) the same leading term $\Delta\delta^{PA}$, the jump in the δ -parameter of the background ^{PA} medium. This parameter $\Delta\delta^{PA}$ should be included in all azimuthally isotropic AVO analyses, particularly at shale-sand interfaces. By the logic above, it may make a significant contribution to the AVO gradient, even though it is small compared to one. Hence, conventional isotropic AVO analysis, which typically neglects this term, is subject to significant uncertainty.

For such azimuthally isotropic cases, the evaluation of the term $\Delta\delta^{PA}$ is difficult, since it may have similar magnitude to the other terms in the conventional isotropic AVO reflectivity gradient. However, a feasible data-driven algorithm for evaluating this term was given by Lin and Thomsen (2013). In azimuthally isotropic cases, this algorithm requires access to log data from a nearby borehole. But, in the present case of fractured media, the effect of the anisotropic term is immediately obvious in surface seismic data only, as discussed in the next section.

Azimuthal anisotropy

In the present case of fractured shales, the azimuthal differences in anisotropic parameters are directly proportional to the nondimensional fracture compliances, a result of the present assumptions:

$$\varepsilon_{23} - \varepsilon_{13} \approx 2\delta_N \left(1 - \frac{C_{66}^{PA}}{C_{11}^{PA}} \right) \frac{C_{66}^{PA}}{C_{33}^{PA}} \quad (6a)$$

$$\delta_{23} - \delta_{13} \approx \frac{\delta^{PA} \delta_V C_{55}^{PA}}{(C_{33}^{PA} - C_{55}^{PA})} + \frac{\delta_N C_{13}^{PA} (1-g) (C_{13}^{PA} + C_{55}^{PA}) + \delta_V C_{55}^{PA} (C_{13}^{PA} + C_{33}^{PA})}{C_{33}^{PA} (C_{33}^{PA} - C_{55}^{PA})} \quad (6b)$$

If the background anisotropy δ^{PA} is weak, then Eq. (6b) further simplifies substantially:

$$\delta_{23} - \delta_{13} = \delta_N (1-g) \left(1 - 2 \frac{C_{55}^{PA}}{C_{33}^{PA}} \right) + 2\delta_V \frac{C_{55}^{PA}}{C_{33}^{PA}} \quad (6c)$$

This difference (6bc) drives the azimuthal differences in reflectivity gradient (*cf.* equations (5ab):

$$R_2^{23} - R_2^{13} \approx \frac{1}{2} [\Delta\delta_{23} - \Delta\delta_{13}] \quad (7)$$

which can lead to significant azimuthal differences in AVO behavior, so-called AVOAz behavior. It is common to observe azimuthal differences in reflection amplitudes; the most plausible interpretation often involves oriented fractures, such as those modelled here.

The Logical Error in Gassmann Poroelasticity: Experimental Data

Leon Thomsen

University of Houston, 77204, Houston, Texas, USA

Contact email: lathomsen@uh.edu

Introduction

A logical error was recently discovered in Gassmann's (1951) derivation of his well-known expression for the fluid-dependence of porous rock incompressibility. Without this error, the fluid-dependence of porous rock incompressibility contains an additional parameter, which is specified below as the parameter κ_M of Brown and Korringa (1975), different than the Solid compressibility κ_S . Limited data is presented below, show that these two parameters are actually different, at least for Berea sandstone.

Gassmann (1951)

The essential result of Gassmann (1951), relating the undrained and frame incompressibilities of a macro-isotropic porous rock, is given here in modern notation:

$$K_{ud} = K_{fr} + \frac{(1 - K_{fr} K_S^{-1})^2}{\phi(K_F^{-1} - K_S^{-1}) + (1 - K_{fr} K_S^{-1}) K_S^{-1}} \quad (1)$$

where the subscripts indicate respectively the incompressibility K of the undrained (*ud*) rock, the frame (*fr*) of the rock, the Solid (*S*) grains of the rock, and the Fluid (*F*) in the pore space of the rock; ϕ is porosity. This result has been used extensively to help understand the fluid content of subsurface rocks.

Gassmann's expression (1) may be re-written exactly in terms of compressibilities $\kappa = 1/K$ as:

$$\kappa_{ud} = \kappa_{fr} - \frac{(\kappa_{fr} - \kappa_S)^2}{\phi(\kappa_F - \kappa_S) + \kappa_{fr} - \kappa_S} \quad (2)$$

As described by Thomsen (2021) and references cited therein, Gassmann's derivation of (1, 2) contained a logical error: a theorem valid for a hydraulically open rock system, was applied to the hydraulically closed system of wave propagation. Details of the error implementation and its ramifications are given there, and are not repeated here. This error was **not** made by Biot (1941), nor by Brown and Korringa (1975), hence their (mutually equivalent) results, corresponding to (2), contain an additional parameter.

Brown and Korringa (1975) ("B&K")

B&K's (correct) derivation of the relation between κ_{ud} and κ_{fr} may be written (Thomsen 2021 *etc*) as:

$$\kappa_{ud} = \kappa_{fr} - \frac{(\kappa_{fr} - \kappa_M)^2}{\phi(\kappa_F - \kappa_S) + \kappa_{fr} + \kappa_S - 2\kappa_M} \quad (3)$$

where κ_M is the Mean of the Solid and pore compressibilities (*cf.* B&K p. 614).

B&K's derivation relaxed Gassmann's assumption of micro-homogeneous Solid, and they thought that this was responsible for the additional parameter. They argued (their p. 610) that, in Gassmann's special case of micro-homogeneous Solid, $\kappa_M = \kappa_S$, so that their result (3) reduced to Gassmann's result (2), thus establishing consistency with Gassmann for this case. However, that particular argument (p. 610) by B&K violated their own assumption of a hydraulically closed system, and so is

not correct; this is similar to the logical error made by Gassmann. **Hence, equation (3) should be used instead of equation (1) or (2) to analyse the fluid dependence of all isotropic rock elasticity.**

Hart and Wang (2010)

In order to verify these theoretical conclusions, it is necessary to experimentally measure both κ_S and κ_M on many rocks, under many pressure conditions. This requires quasi-static (not ultrasonic) measurements, since the theory is explicitly valid only at low frequencies.

κ_S may be determined with an “unjacketed” compression experiment, where the bulk strain results from equal pressure on all sides of the grains of the rock. This (open-system) procedure is legitimate in this closed-system context, since the Solid compressibility is the same in open and closed systems.

κ_M may be determined via direct measurement of $B = dp_F / dp$, undrained (Thomsen, 2021 *etc.*):

$$\kappa_M = \kappa_{fr} - \frac{(\kappa_{fr} - \kappa_{ud})}{B} \quad (4)$$

The quasi-static data of Hart and Wang (2010) for Berea sandstone, as a function of differential pressure, $p_d = p - p_F$, are shown below. The Mean compressibility κ_M shows a difference from the Solid compressibility κ_S , statistically significant (as much as 20%), and pressure-dependent.

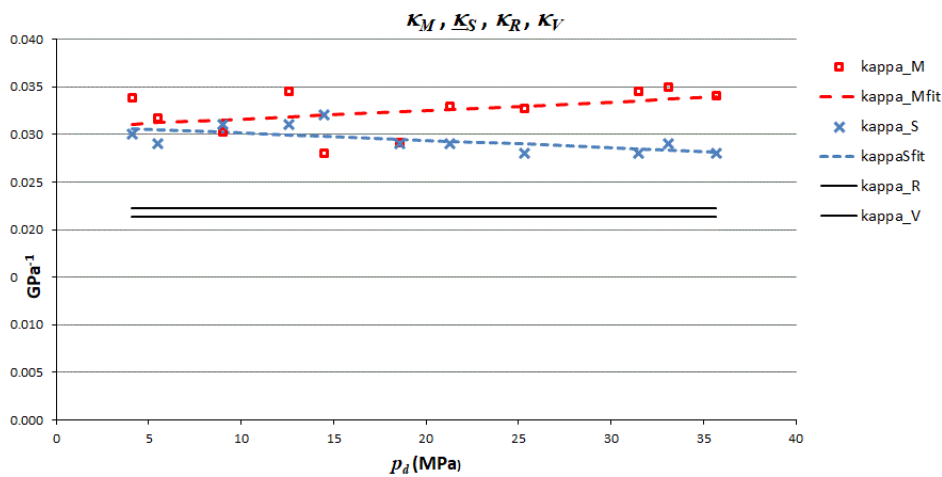


Figure 1. Data on Berea sandstone from Hart and Wang (2010).

References

- Biot, M A (1941) *General theory of three-dimensional consolidation. J. Appl. Phys.* 12, 155-164.
- Brown, R J S, and Korrington, J. (1975) *On the dependence of the elastic properties of a porous rock on the compressibility of the pore fluid. GEOPHYSICS* 40, 608-616.
- Gassmann, F (1951) *Über die Elastizität poroser Medien. Mitteilungen Inst. Geophysik (Zurich)* 17, 1-23. Translated as: *On elasticity of porous media, in Classics of Elastic Wave Theory, M A Pelissier, Ed., Soc. Expl. Geoph., Tulsa, 2005.*
- Hart, D J and H F Wang (2010) *Variation ofunjacketed pore compressibility using Gassmann’s equation and an overdetermined set of volumetric poroelastic measurements. GEOPHYSICS* 75, N9–N18.
- Thomsen, L (2021) *The Logical Error in Gassmann Poroelasticity: Consistency with Effective Medium Theory. Soc. Expl. Geoph. Expnd. Absts.* 91, 2303-2307.